EPJ manuscript No.
(will be inserted by the editor)

Complex band-structure analysis and topological physics of Majorana nanowires

Javier Osca[1,2a] and Llorenç Serra[3,4b]

[1] IMEC, Kapeldreef 75, B-3001 Leuven, Belgium
[2] KU Leuven, ESAT-MICAS, Kasteelpark Arenberg 10, 3001 Leuven, Belgium
[3] Institut de Física Interdisciplinària i de Sistemes Complexos IFISC (CSIC-UIB), E-07122 Palma, Spain
[4] Departament de Física, Universitat de les Illes Balears, E-07122 Palma, Spain

Received: date / Revised version: date

Abstract. We review applications of complex band structure theory to describe Majorana states in nanowires and nanowire junctions. The dimensionality of the considered wires is gradually increased, from strictly 1D to quasi-1D with one and two transverse dimensions. The complex wave number analysis is applied to two main types of Majorana modes: end states in hybrid semiconductor wires and chiral edge states in hybrid wires of quantum-anomalous Hall insulators. In topological NS and NSN junctions with Majorana modes conductance oscillations and spatial distributions of density and current are described. Finally, the optical absorption in finite systems with both types of Majorana modes is considered.

PACS. 72.10.-d Electronic transport in condensed matter 73.63.Nm Quantum wires 74.45.+c Superconductivity

1 Introduction

In this paper we review our recent applications of complex band structure to describe low dimensional states appearing near the edges or interfaces between different types of topological materials. We mostly refer to hybrid nanowires formed when a semiconductor wire is put in close proximity to a superconductor material such that superconductivity is transferred to the quasiparticles of the nanowire. These systems are a class of topological devices, with phases having a characteristic number of low-dimensional states, Majorana zero modes attached to the nanowire ends. Such states have attracted an enormous interest in recent years as they are a Condensed Matter realization of the elementary particles envisaged by E. Majorana many years ago [1]. Measurement of zero-bias anomalies of NS junctions, with quantized conductance peaks $2e^2/h$, have indeed provided solid evidence on the reality of such quasiparticles [2–8].

Several review papers have already addressed the topic of Majorana modes in Condensed Matter systems [9–14]. For that reason, the purpose of this work is to more directly focus specifically on the description of Majorana states using complex band structure theory. We describe below our works based on this approach for topological quantum wires and nanowire junctions hosting Majorana states. Since low-dimensional topological states are not propagating in the bulk, band structure theory has to be generalized to describe evanescent states, fading away with the distance to the interface. This is achieved with the complex band structure in which the wave number is generalized to have real and imaginary parts $k = k_r + ik_i$ [15–18]. The imaginary part k_i allows to model exponentially decaying behaviour with increasing distance to the interface, a needed property for the characterization of general low-dimensional states confined along some directions. An important difference with theoretical approaches based on the evaluation of topological invariants obtained with bulk states, complex band theory allows modelling specific interfaces in nanowires by directly calculating energy and wave function of the low-dimensional states.

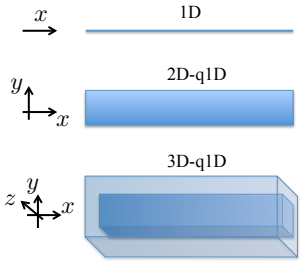

Fig. 1. Schemes of infinite q1D nanowires along x with different numbers of transverse dimensions: none, y or yz.

[a] *e-mail:* javier.osca@imec.be
[b] *e-mail:* llorens.serra@uib.es

We consider nanowires, with the nanowire axis along x, with a strong confinement in the transverse directions. The wavenumber k is thus associated with translational invariance along x. Depending on the number of transverse confined degrees of freedom we consider 2D (x, y) and 3D (x, y, z) models. These cases will be referred to by the acronyms 2D-q1D and 3D-q1D for nanowire models having y and yz transverse degrees of freedom, respectively, with q1D for quasi-one dimensional system. Of course, strict 1D wires with only one degree of freedom x will also be discussed. 2D-q1D wires are often called ribbons, strips or stripes in the literature. The complex band analysis is first applied to each of these q1D models, in order to determine the set of complex k's and transverse states. Subsequently, these results are applied to describe inhomogeneous junctions of the normal-superconductor-normal (NSN) type by solving the proper matching conditions of the solutions for the different regions

Besides the localized Majorana attached to the ends of hybrid semiconductor wires, we will also discuss propagating Majorana states along the edges of 2D-q1D hybrid topological insulators that have recently attracted much interest [19–21]. These type of Majoranas are formed in quantum-anomalous-Hall topological insulators and they are chiral, with a well defined sense of rotation along the edges of the system [22–30].

This review is organized as follows:

1. **Introduction** presenting the general idea and purpose of the review paper.
2. **Methodology and 1D**. In Sec. 2 we review two methods to calculate the complex wave numbers $k(E)$ of a 1D hybrid nanowire at a particular energy E. The first method is based on the evaluation of a continuity measure, represented by a function $\mathcal{F}(k)$, while the second one consists in diagonalizing a non Hermitian matrix having $k(E)$ as its corresponding eigenvalues. These methods will be used to determine the Majorana phase limits defining a critical value of the Zeeman parameter and critical angles of the magnetic field orientation. It is also shown how complex-k solutions are used to explicitly obtain the Majorana wave function.
3. **k-analysis in 2D-q1D**. This Section extends the preceding one to 2D-q1D devices. The analysis based on $\mathcal{F}(k)$ is particularly useful to determine the Majorana phases because Majorana phase transitions occur when the gap closes and reopens at $k = 0$ only. On the other hand, the Majorana wave function is obtained imposing the edge condition $\Psi(x = 0, y) = 0$. A key point is that the Majorana wave function can be rewritten as a linear superposition of the eigenstates of the equivalent infinite nanowire for different $k(E)$. We can obtain the wave number and wave function of these states by the same non-Hermitian matrix methods presented in Sec. 3. These numerical methods are also used to study the Majorana phase boundaries and wave functions in presence of orbital effects.
4. **k-analysis in 3D-q1D**. This Section further extends the two preceding ones to a 3D-q1D nanowire. The key point is that now a transverse cut of the 3D wire is a full 2D section with many possible shapes (Fig. 1). We focus on prismatic-shaped nanowires, where quasiparticles localize on the facets of the wire shell, with effective q1D wires emerging along the prism edges. Orbital effects due to the magnetic field are also considered.
5. **NS junctions in 2D-q1D**. In this Section we study Majorana nanowire junctions between normal and superconducting sections. The matching condition on the junction edge is obtained by a set of grid equations connecting the normal and the superconductor sides. The method is used to calculate the conductance and current density at the junction in presence and absence of a Majorana mode. It is shown how magnetoconductance oscillations, typical of trivial NS junctions, are suppressed when the superconductor is in the topological state.
6. **Conductance oscillations with chiral Majoranas**. This Section discusses transport features of a chiral Majorana device. It is shown how transverse finite size effects lead to characteristic conductance oscillations, either with applied bias or with system length. We stress that measuring those oscillations amounts to determining the speed of the chiral Majorana modes in an interferometer-like operation of the device.
7. **Optical absorption** of both end-localized and chiral Majorana modes in nanowires. For both types, characteristic absorption features due to the presence of the Majorana modes are identified.
8. **Conclusions.** Finally, an outlook of the whole review is presented with a summary of key results.

2 Methodology and 1D

As a first step towards piecewise-homogeneous junctions in quantum wires, we have to determine the complex band structure for an infinite wire with the constant parameters of each region [18]. We illustrate the method in this section with the 1D case, where we assume the Hamiltonian

$$\mathcal{H}_{1D} = \left(\frac{p_x^2}{2m} - \mu\right)\tau_z + \Delta_B\,\boldsymbol{\sigma}\cdot\hat{n} + \Delta_0\,\tau_x + \frac{\alpha}{\hbar}\,p_x\sigma_y\tau_z\ . \tag{1}$$

The Pauli operators for spin and isospin (in electron-hole space) are represented in Eq. (1) by the σ and τ vector operators, respectively. The different energy contributions are kinetic, Zeeman (Δ_B), pairing (Δ_0) and Rashba spin-orbit coupling (α). In addition, Eq. (1) also includes the chemical potential (μ) and the magnetic field orientation ($\hat{n}$). The system exhibits very different physics for parallel ($\hat{n} = \hat{x}$) and transverse ($\hat{n} = \hat{y}, \hat{z}$) field orientations. Since in 1D all transverse orientations with the same relative angle between $\hat{n}$ and $\hat{y}$ are equivalent, it is enough to consider fields in the xy plane, with an azimuthal angle $0 \le \phi_B \le 2\pi$.

The band structure is obtained from Schrödinger equation

$$\mathcal{H}_{1D}\,\Psi(x, \eta_\sigma, \eta_\tau) = E\,\Psi(x, \eta_\sigma, \eta_\tau)\ , \tag{2}$$

where space coordinate $x \in (-\infty, +\infty)$, spin $\eta_\sigma \in \{\uparrow, \downarrow\}$ and isospin $\eta_\tau \in \{\Uparrow, \Downarrow\}$. Introducing a state wave number k we expand

$$\Psi(x, \eta_\sigma, \eta_\tau) = \sum_{s_\sigma s_\tau} \psi^{(k)}_{s_\sigma s_\tau} \; e^{ikx} \, \chi_{s_\sigma}(\eta_\sigma) \, \chi_{s_\tau}(\eta_\tau) \; , \qquad (3)$$

where $s_\sigma = \pm$, $s_\tau = \pm$ and the spin/isospin basis states fulfill

$$\boldsymbol{\sigma} \cdot \hat{n} \, \chi_{s_\sigma}(\eta_\sigma) = s_\sigma \, \chi_{s_\sigma}(\eta_\sigma) \; , \qquad (4)$$

$$\tau_z \, \chi_{s_\tau}(\eta_\tau) = s_\tau \, \chi_{s_\tau}(\eta_\tau) \; . \qquad (5)$$

The amplitudes $\psi^{(k)}_{s_\sigma s_\tau}$ in Eq. (3) can be viewed as a set of four complex numbers representing the state for a given wave number k. Substituting Eq. (3) in Eq. (1) we easily get the equations for the state complex amplitudes $\psi_{s_\sigma s_\tau}$ (we drop label k for convenience)

$$\left[\left(\frac{\hbar^2 k^2}{2m} - \mu\right) s_\tau + \Delta_B s_\sigma + \alpha k \, s_\sigma s_\tau \sin\phi_B - E\right] \psi_{s_\sigma s_\tau} + \Delta_0 \, \psi_{s_\sigma \overline{s}_\tau} + i\alpha k \, s_\sigma s_\tau \cos\phi_B \, \psi_{\overline{s}_\sigma s_\tau} = 0 \; , \qquad (6)$$

where $\overline{s} = -s$. Equation (6) is an algebraic (matrix) equation with nondiagonal couplings of $\psi_{s_\sigma s_\tau}$ to $\psi_{s_\sigma \overline{s}_\tau}$ through pairing and to $\psi_{\overline{s}_\sigma s_\tau}$ through the Rashba interaction.

With a given energy E, Eq. (6) determines a set of solutions for k reflecting the band structure. An allowed k which is purely real describes a propagating state while a complex k with nonvanishing imaginary part describes an evanescent state. Finding the physically allowed k's at a given energy E, even numerically, is a non trivial task. Notice, for instance, that the matrix in Eq. (6) is non Hermitian for an arbitrary complex k. While many numerical methods can deal with Hermitian matrices (e.g., Ref. [31]), the methods for non Hermitian operators are scarce.

A possible method to determine the allowed k's, devised in Refs. [18,32] introduces a measure $\mathcal{F}(k)$ of the deviation from fulfilling Eq. (6), such that the physically allowed k's are found by sweeping the complex k plane looking for the zeros $\mathcal{F}(k) = 0$. Another possibility to determine the set of k values is to use numerical diagonalization methods for non Hermitian matrices [33]. By a clever transformation [34], enlarging the number of components of the wave function $\psi_{s_\sigma s_\tau} \to \tilde{\psi}_{s_\sigma s_\tau s_g}$ with $s_g = \pm$, as

$$\tilde{\psi}_{s_\sigma s_\tau s_g} = \begin{cases} \psi_{s_\sigma s_\tau} & \text{if } s_g = + \; , \\ k \, \psi_{s_\sigma s_\tau} & \text{if } s_g = - \; , \end{cases} \qquad (7)$$

Eq. (6) transforms into a linear eigenvalue problem for k and $\tilde{\psi}_{s_\sigma s_\tau s_g}$. The corresponding matrix is non Hermitian, as could have been anticipated in order to allow for complex k's. We have diagonalized it with the ARPACK package for nonHermitian sparse eigenvalue problems [33].

Figure 2 shows an illustrative example of 1D band structure in effective units $E_{SO} = \alpha^2 m/\hbar^2$, $L_{SO} = \hbar^2/\alpha m$. For a fixed energy there are always eight modes; some

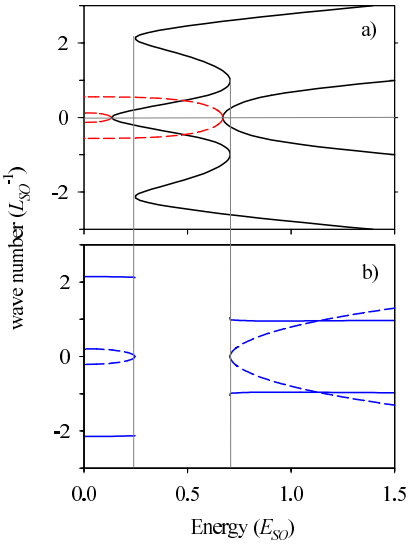

Fig. 2. Complex band structure of a 1D illustrative case. Solid and dashed lines correspond to real and imaginary wavenumbers, respectively. Panel a) shows purely real and purely imaginary modes. Panel b) shows mixed modes having both real and imaginary contributions to the wave number. Thin gray lines are guides helping the eye to correlate the position of the band extrema. Parameters: $\Delta_B = 0.4 E_{SO}$, $\Delta_0 = 0.25 E_{SO}$, $\mu = 0.1 E_{SO}$, $\phi_B = \pi/4$. From [18].

of them are purely real ($k = k_r$) or purely imaginary ($k = ik_i$) shown in Fig. 2a; while others have both contributions ($k = k_r + ik_i$), shown in Fig. 2b. For vanishing E's all modes are evanescent, while for large E's we have 4 purely real and 4 mixed modes. Notice that band extrema correspond to transformations of one type of mode into another such that k_i always vanishes smoothly in a transition.

The evanescent modes are essential for the description of localized states in 1D, fading away from a given point. For a semi infinite segment $x \geq 0$, the condition of a vanishing wave function at $x = 0$ is then

$$\sum_{k \in \{\tilde{k}\}} C_k \, \psi^{(k)}_{s_\sigma s_\tau} = 0 \; , \qquad (8)$$

where the C_k's are complex numbers and the $\psi^{(k)}_{s_\sigma s_\tau}$'s are the state amplitudes defined above. The set $\{\tilde{k}\}$ is the number of evanescent modes with $\Im(k) > 0$ and has to contain at least $\tilde{N} = 4$ modes, since otherwise only the trivial solution $C_k = 0$ is possible. Even in cases when $\tilde{N} = 4$, the existence of an end state is still not guaranteed, since it also has to be fulfilled

$$\det\{\psi^{(k)}_{s_\sigma s_\tau}\} = 0 \; . \qquad (9)$$

Figure 3 shows that the determinant Eq. (9) vanishes consistently when the Zeeman parameter exceeds a critical value. It corresponds to the vanishing of the imaginary part k_i for two of the modes, while $k_r = 0$ also. That is, $k = 0$ becomes a physical solution but only for this

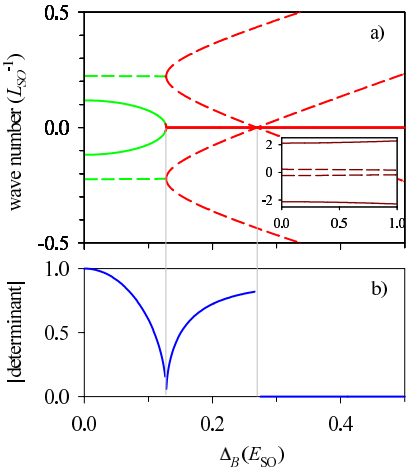

Fig. 3. a) Complex band structure for a fixed $E = 0$ and rest of parameters as in Fig. 2. The inset shows the modes with a large value of $\Re(k)$. b) Absolute value of the determinant Eq. (9). A vanishing determinant is the condition for the existence of an end state. From [18].

particular Δ_B. This is an example of phase transition, signaled by the $k = 0$ gap closing and reopening as Δ_B is increased. The relevance of the $k = 0$ gap closing for the determination of the phase boundaries was stressed in Ref. [35]. The phase transition in parallel field is characterized bu a critical Zeeman parameter

$$\Delta_B^{(c)} = \sqrt{\Delta_0^2 + \mu^2}\,, \tag{10}$$

such that zero-energy edge (Majorana) modes are present only when $\Delta_B > \Delta_B^{(c)}$.

The above is an example of the use of complex band structure to determine the phase transition to a Majorana end state in 1D. The Majorana state density, defined as

$$\rho(x) \equiv \sum_{s_\sigma s_\tau} \rho_{s_\sigma s_\tau}(x)\,,$$
$$\rho_{s_\sigma s_\tau}(x) = \sum_{kk'} C_{k'}^* C_k\, \psi_{s_\sigma s_\tau}^{(k')*} \psi_{s_\sigma s_\tau}^{(k)} e^{i(k-k'^*)x}\,, \tag{11}$$

can easily be obtained once the C_k coefficients are known. Figure 4 shows the density profile for a particular set of parameters, proving the edge character of the mode which, in general, presents a combinations of oscillating a decaying behaviors.

Tilted orientations of the magnetic field, given by polar angles (θ, ϕ) (see Fig. 5) were studied in Ref. [36]. It was found that the phases of Majorana zero modes are characterized by an additional rule, besides Eq. (10). Specifically, the following two conditions are to be met simultaneously

$$\Delta_B > \sqrt{\Delta_0^2 + \mu^2}\,, \tag{12}$$
$$\Delta_B \sin\theta\, |\sin\phi| < \Delta_0\,. \tag{13}$$

Equation (13) was named the projection rule in Ref. [36] since it reflects the condition that the Zeeman term

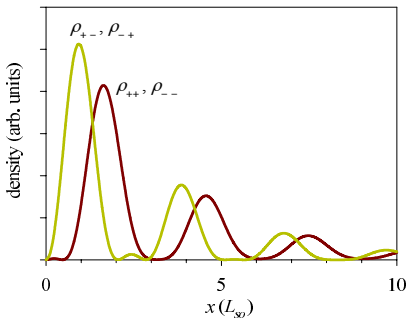

Fig. 4. Density distributions for a Majorana state with zero energy, defined in Eq. (11). The rest of parameters are as in Fig. 2. From [18].

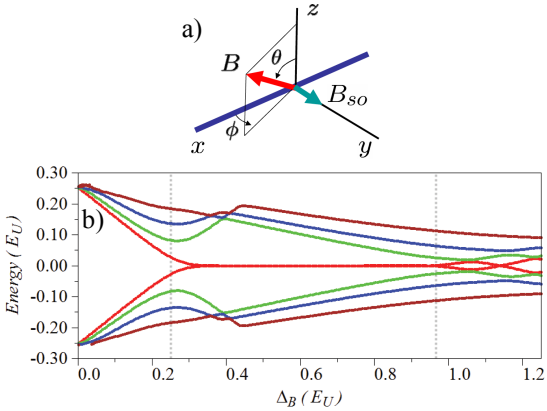

Fig. 5. a) Sketch of a 1D wire in a tilted field. b) Energy spectrum of a finite 1D wire of length $L = 50L_{SO}$ in a tilted field as a function of the Zeeman parameter Δ_B. The two vertical lines indicate the transition values of Δ_B obtained by complex wavenumber analysis, Eqs. (12) and (13). The spectrum of eigenenergies is obtained by diagonalization of the nanowire Hamiltonian Eq. (1) using finite differences. The energy unit is $E_U = E_{SO}$. Parameters: $\theta = 90°$, $\phi = 15°$, $\Delta_0 = 0.25E_{SO}$ and $\mu = 0$. From [36].

projected on the perpendicular direction to the wire (y) has to be smaller than the pairing energy. Physically, this condition corresponds to the indirect gap closing at finite k's that leads to damping of the Majorana mode into propagating states. Figure 5 shows how the two transition boundaries are well fulfilled in a finite length 1D segment: the gap closes at the first transition, Eq. (12), and the zero modes is present up to the second transition given by Eq. (13).

3 k-analysis in 2D-q1D

In this section we extend the 1D analysis to the 2D-q1D nanowire. The model has now two spatial dimensions (x, y)

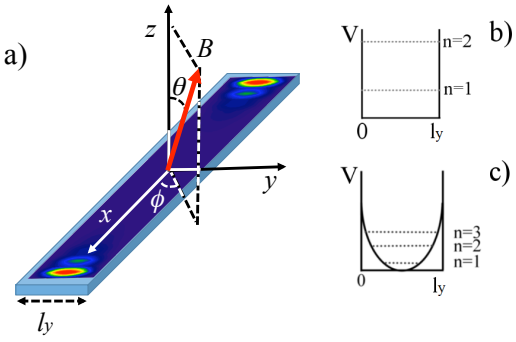

Fig. 6. a) Schematic of a 2D planar nanowire showing the axis definitions and the magnetic field orientation. The density distribution of Majorana modes on the wire ends is qualitatively shown. Transverse potential and energies in the limits of vanishing and large orbital effects are shown in b) and c), respectively. Adapted from Ref. [41].

and the Hamiltonian reads

$$\begin{aligned}\mathcal{H} = &\left(\frac{p_x^2+p_y^2}{2m} + V(x,y) - \mu\right)\tau_z \\ &+ \Delta_B\,\boldsymbol{\sigma}\cdot\boldsymbol{n} + \Delta_0\,\tau_x \\ &+ \frac{\alpha}{\hbar}\,(p_x\sigma_y - p_y\sigma_x)\,\tau_z\,. \end{aligned} \tag{14}$$

We assume a transverse square well potential of width l_y defining transverse energy bands in the nanowire ϵ_n (see Fig. 6b). For this reason, sometimes these nanowires are also referred to as multi-band nanowires [37–39]

In comparison with the 1D nanowire Hamiltonian two p_y dependent terms have been added in Eq. (14); the kinetic and Rashba terms respectively. The latter is named Rashba mixing because it couples different transverse bands of the nanowire [37–40]. If we restrict to in-plane components orbital field effects are absent and, if the width of the nanowire is much smaller than the Rashba length $l_y << l_\alpha \equiv \hbar^2/m\alpha$, the Rashba mixing becomes negligible [38,41]. In this limit each of the bands behaves as an independent 1D nanowire. Each one of these bands fulfills a topological transition rule with critical value $\Delta_{B,n}^{(c)} = \sqrt{\mu_{eff}^2 + \Delta_0^2}$ as in a 1D Majorana nanowire but with an effective chemical potential $\mu_{eff} = \mu - \epsilon_n$ modified by the band energy.

On the other hand, wider nanowires or with a weak spin orbit coupling $l_y \approx l_\alpha$ need a more general approach, especially if the magnetic field points in an arbitrary direction. In this case we use the k-analysis again. Note that a magnetic field component perpendicular to the nanowire surface will affect electron motion in a planar geometry. We include the orbital effects in the Hamiltonian through the minimal substitution $p_x \to p_x - \hbar y/l_z^2\tau_z$, where l_z is the magnetic length defined as $l_z^2 = \hbar c/eB_z$.

Bulk to edge correspondence relates the properties of finite or semi-infinite nanowires holding end Majoranas with the band structure of equivalent infinite nanowires having the same Hamiltonian except for the edges. In particular we can determine the topological phase transition using the band structure of an infinite nanowire. The eigensolutions of the infinite nanowire with a given wavenumber k read

$$\Psi^{(k)}(x,y,\eta_\sigma,\eta_\tau) = \sum_{s_\sigma s_\tau} \Psi^{(k)}_{s_\sigma s_\tau}(y)\, e^{ikx}\, \chi_{s_\sigma}(\eta_\sigma)\, \chi_{s_\tau}(\eta_\tau)\,, \tag{15}$$

generalizing Eq. (3) to y-dependent spinors $\Psi^{(k)}_{s_\sigma s_\tau}(y)$. The equation yielding the full 2D-q1D band structure is now

$$\sum_{s'_\sigma s'_\tau} \langle s_\sigma s_\tau | h(k) | s'_\sigma s'_\tau \rangle\, \Psi^{(k)}_{s'_\sigma s'_\tau}(y) = E\, \Psi^{(k)}_{s_\sigma s_\tau}(y)\,, \tag{16}$$

where

$$\begin{aligned} h(k) = &\left(\frac{\hbar^2k^2+p_y^2}{2m} + V(y) - \mu\right)\tau_z + \Delta_0\,\tau_x \\ &+ \frac{\alpha}{\hbar}\,(\hbar k\sigma_y - p_y\sigma_x)\tau_z \\ &+ \Delta_B\,\hat{\sigma}\cdot\hat{n} + \frac{\hbar^2}{2ml_z^4}y^2\tau_z - \frac{\alpha}{l_z^2}y\sigma_y \end{aligned} \tag{17}$$

is a k-dependent effective 1D Hamiltonian. Note that we assumed the Landau gauge centered on $y_c = 0$ for the orbital terms in order to obtain a simpler expression.

In 1D nanowires a Majorana phase transition is signaled by the closing and reopening of the gap at $k = 0$. We assume that this is still true for 2D-q1D and, later on, we explicitly check the correctness of this hypothesis. This assumption relies on previous works [38,37] and the proven fact that in certain conditions each of the nanowire bands behaves like an independent 1D nanowire. Therefore, to determine the phase boundaries we do not need the full band structure but only Eq. 16 for $k = 0$. That is,

$$\sum_{s'_\sigma s'_\tau} \langle s_\sigma s_\tau | h(0) | s'_\sigma s'_\tau \rangle\, \Psi^{(0)}_{s'_\sigma s'_\tau}(y) = E\, \Psi^{(0)}_{s_\sigma s_\tau}(y)\,. \tag{18}$$

This equation can be solved analytically for two limiting cases: when the nanowire is in a longitudinally oriented magnetic field and in the regime of strong orbital effects with large perpendicular components of the magnetic field. These are two limiting test cases for the more general numerical method. The two analytic regimes and the numerical method are explained next.

3.1 Regime of longitudinal magnetic field

With field along the longitudinal axis of the nanowire $l_z^{-2} = 0$ and the orbital terms can be neglected. In this particular case Majorana phase boundaries are analytical by solving Eq. (18). Furthermore, the potential term $V(y)$ is also removed from Eq. (18) because we consider a square well confinement with zero potential inside. The effective 1D Hamiltonian becomes,

$$h = \left(\frac{p_y^2}{2m} - \mu\right)\tau_z + \Delta_0\,\tau_x + \left(\Delta_B - \frac{\alpha}{\hbar}p_y\tau_z\right)\sigma_x\,, \tag{19}$$

where $h \equiv h(0)$. The equation may be further simplified by absorbing the linear p_y term from the Rashba interaction into the kinetic term,

$$h = \left(\frac{\tilde{p}_y^2}{2m} - \frac{m\alpha^2}{2\hbar^2} - \mu \right) \tau_z + \Delta_0 \, \tau_x + \Delta_B \sigma_x \, , \qquad (20)$$

where $\tilde{p}_y = p_y - m\alpha\sigma_x/\hbar$. A simple way to solve Eq. (20) is rewriting it in matrix form using a basis of square-well eigenstates of energies $\epsilon_n = \hbar^2\pi^2 n^2/(2ml_y^2)$ as

$$h \equiv \begin{pmatrix} \epsilon_n - \mu - \frac{m\alpha^2}{2\hbar^2} + \Delta_B\sigma_x & \Delta_0 \\ \Delta_0 & -(\epsilon_n - \mu - \frac{m\alpha^2}{2\hbar^2}) + \Delta_B\sigma_x \end{pmatrix} . \qquad (21)$$

The eigenenergies of matrix Eq. (21) are

$$E_n = \pm\Delta_B \pm \sqrt{\left(\mu - \epsilon_n + \frac{m\alpha^2}{2\hbar^2} \right)^2 + \Delta_s^2} \, . \qquad (22)$$

The $k = 0$ gap closing corresponds to the zero eigenvalue and, therefore, to critical Zeeman parameters

$$\Delta_{B,n}^{(c)} = \sqrt{\left(\mu - \epsilon_n + \frac{m\alpha^2}{2\hbar^2} \right)^2 + \Delta_s^2} \, . \qquad (23)$$

The result of (23) is valid for not extremely narrow nanowires where the Rashba mixing term is relevant. From a physical point of view this has two important consequences. First, the critical magnetic field for each transverse band is explicitly modified by an α dependent term. See Fig. 7 for a non trivial phase diagram if we assume a tunable α by an external electric field. On the other hand, the Rashba mixing term makes the Majorana modes of each of the transverse bands see each other annihilating them in pairs. Therefore an alternation between trivial and topological single Majorana mode phases are found in the phase diagram when an even or odd number of bands are above the critical magnetic field respectively.

3.2 Regime of strong orbital effects

The other limiting case is the strong orbital limit. The planar nanowire is in the strong orbital limit when $l_z \ll l_y \ll l_\alpha$. With these conditions the y^2 dependent orbital term behaves as an effective harmonic confining potential for the Majorana mode (see Fig. 6c). Therefore, in Eq. (17) the potential $V(y)$ and the Rashba terms become negligible, resulting in the effective 1D Hamiltonian

$$h(0) = \left(\frac{p_y^2}{2m} + \frac{\hbar^2}{2ml_z^4} y^2 - \mu \right) \tau_z + \Delta_B \, \boldsymbol{\sigma} \cdot \hat{n} + \Delta_0 \, \tau_x \, . \qquad (24)$$

In a harmonic-oscillator basis, the matrix of Eq. (24) reads

$$\begin{pmatrix} \epsilon_n^{(ho)} - \mu + \Delta_B & \Delta_0 \\ \Delta_0 & -\left(\epsilon_n^{(ho)} - \mu \right) + \Delta_B \end{pmatrix} , \qquad (25)$$

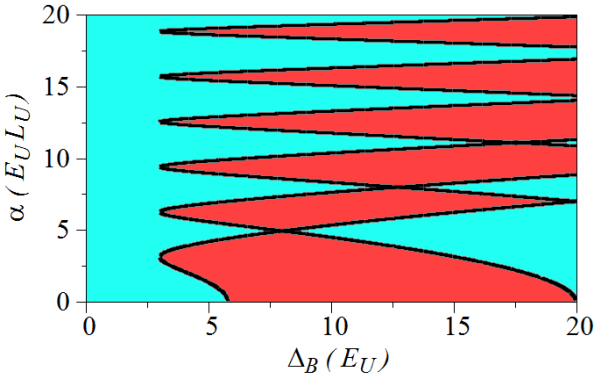

Fig. 7. a) Phase transition boundaries for a 2D planar nanowire with a longitudinal (x) magnetic field. We have assumed $\Delta_0 = 3E_U$ and $\mu = 0$. The red regions correspond to topological phases with a Majorana zero mode while the light blue ones correspond to trivial ones. The units are $L_U = l_y$ and $E_U = \hbar^2/ml_y^2$. From [41].

where $\epsilon_n^{(ho)} = (n-1/2)\hbar^2/ml_z^2$ are the harmonic oscillator energies. Note that we have intentionally labeled the energies as $n = 1, 2...$, instead of the more usual $n = 0, 1, 2....$ The reason will be obvious in the next subsection. The condition of zero eigenvalue is

$$\Delta_B = \sqrt{\left[(n - 1/2)\frac{\hbar^2}{ml_z^2} - \mu \right]^2 + \Delta_0^2} \, . \qquad (26)$$

In spite of the similarity of Eq. (26) with Eq. (23), there are deep differences. A closer look reveals that there is a Δ_B dependence on the r.h.s. of Eq. (26) through $l_z^2 = \frac{\hbar^2 g m^*}{4m\Delta_B \cos\theta}$ where m^* is the ratio of effective to bare mass ($m = m^* m_e$) and g is the gyromagnetic factor. The gyromagnetic factor gives the Zeeman coupling with the magnetic field strength $\Delta_B \equiv g\mu_B B/2$. Equation (26) can be interpreted as defining critical tilting angles $\theta_n^{(c)}$,

$$\cos\theta_n^{(c)} = \frac{gm^*}{4} \frac{\sqrt{\Delta_B^2 - \Delta_0^2} + \mu}{\left(n - \frac{1}{2}\right)\Delta_B} \, . \qquad (27)$$

Furthermore, if $\Delta_B >> \Delta_0$ and $\Delta_B >> \mu$ this expression can be further simplified to:

$$\cos\theta_n^{(c)} = \frac{gm^*}{4\left(n - \frac{1}{2}\right)} \, . \qquad (28)$$

Note that this last simplification is valid when $l_z << l_s \equiv \sqrt{\hbar^2/m\Delta_0}$.

The effective harmonic confinement depends on the external magnetic field and this leads to Majorana phase boundaries independent of the field strength. In fact, instead of having critical magnetic fields we have critical magnetic angles. That is, if the magnetic field is strong enough the nanowire remains in the Majorana phase independently of the field strength provided that its orientation is kept fixed (see Fig. 8). The obvious question how is the transit between these two limiting phases is answered in the following section.

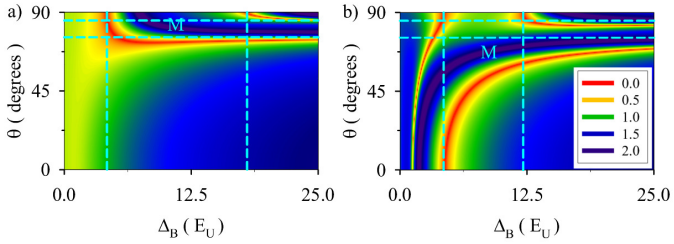

Fig. 8. $\mathcal{F}$ measure in a color scale as a function of Δ_B and polar angle θ. The azimuthal angle remains $\phi = 0$. Zero values of $\mathcal{F}$ (red) signal the phase transition boundaries. Phases with a Majorana mode are labeled with an M. The panels correspond to $\alpha = 0.1\, E_U L_U$ (a) and $4\, E_U L_U$ (b). Dashed lines indicate the analytical limits. We have assumed $\Delta_0 = 3\, E_U$ and typical InAs parameters $g = 15$, $m^* = 0.033$. Figure adapted from [41]

3.3 General numerical method

In the preceding two sections we have obtained analytical expressions of the Majorana phase boundaries in two particular regimes: critical $\Delta_{B,n}^{(c)}$ in longitudinal fields and critical $\theta_n^{(c)}$ in the strong orbital limit. Each case is represented by vertical and horizontal blue dotted lines in Fig. 8 overprinted to the numerically calculated phase boundaries (red). This diagram shows how the analytical solutions are indeed proper limits of the phase boundaries, that bent themselves to adapt from a regime of critical magnetic fields to a regime of critical magnetic angles.

The general diagram of Fig. 8 is obtained using wave number analysis in combination with a y-matching numerical method. A key point is to notice that Eq. (18) is a 1D equation that only depends on the y coordinate. This effective 1D equation yields the transverse wave functions $\Psi^{(0)}_{s_\sigma s_\tau}(y)$ at wavenumber zero as unknowns. Inspired by 1D case, we devise a numerical algorithm to avoid the trivial zero solution. First we discretize Eq. (18) on a uniform grid for all points $(y, s_\sigma, s_\tau) \neq (y_m, s, t)$, where (y_m, s, t) are an arbitrarily chosen matching point and spin-isospin component. We also require

$$\Psi_{st}(y_m) = 1\,, \tag{29}$$

$$\left(\frac{d^{(L)}}{dy} - \frac{d^{(R)}}{dy}\right)\Psi_{s_\sigma s_\tau}(y_m) = 0\,, \quad (s_\sigma, s_\tau) \neq (s, t)\,. \tag{30}$$

The continuity of the wavefunction and its first derivative at the matching point y_m is ensured by the matching algorithm with the only exception of the (s, t) component. This may be tested afterwards by defining a positive measure

$$\mathcal{F} = \left|\left(\frac{d^{(L)}}{dy} - \frac{d^{(R)}}{dy}\right)\Psi_{st}(y_m)\right|^2\,, \tag{31}$$

where $d^{(L,R)}/dy$ are derivatives with only left (L) or right (R) grid neighbours. Eventually, the Majorana phase boundaries are given by the zeroes $\mathcal{F} = 0$, with fixed $k = 0$ and $E = 0$, while sweeping the remaining parameters.

Figure 8 shows the value of $\mathcal{F}$ for different strengths and orientations of the magnetic field. Majorana phase boundaries are determined by those points where $\mathcal{F}$ vanishes (in red). Non-zero values of $\mathcal{F}$ have no other special meaning. Note that this method has the main advantage of being computationally very efficient. In general the computational cost of a diagonalization algorithm is $O(n^3)$ where n is the number of rows (or columns) of the matrix. Therefore, a diagonalization of the Hamiltonian of a finite nanowire in a grid of $n = N_x N_y$ points implies an order $O(N_x^3 N_y^3)$, for a fixed set of all the remaining Hamiltonian parameters. If $N_x \approx N_y \equiv N$ this is $O(N^6)$. By contrast, the $\mathcal{F}$-function method presented above is based on the reduction of the dimensionality of the problem to an effective set of N_y equations. Solving this system of equations reduces the computational complexity to an order $O(N_y^3) \equiv O(N^3)$, or even lower due to matrix sparseness. In fact, it is computationally unfeasible to determine the phase boundaries performing a full $O(N^6)$ diagonalization of the Hamiltonian at each point of parameter space. Of course, Hamiltonian diagonalization provides additional information about above-gap non-topological states not needed to determine the Majorana phase boundaries alone.

It is shown in Fig. 8a that for the selected material parameters Majorana phase boundaries bend gently to adapt to the different limiting cases. That being said, Fig. 8a is for weak Rashba coupling $l_y << l_\alpha$. A common ordering $n = 1, 2..$ of harmonic oscillator and square well eigensolutions allows the same labelling for the two limiting cases. In this manner, the phase boundary can be attributed to the closing and reopening gap at $k = 0$ of a particular n'th transverse band.

Higher Rashba strengths cause large deviations of the Majorana phase boundaries. In Fig. 8a the Rashba orbital term $\alpha y \sigma_y / l_z^2$ is small and, accordingly, a rather smooth change of the Majorana phase boundaries from critical magnetic fields to critical angles is obtained. However, Fig. 8b shows that this is different if the Rashba strength is large. A large Rashba strength may be due to the intrinsic material or to an external electric field. Besides, varying the nanowire width l_y also changes the relative importance of the Rashba term and transverse confinement in the Hamiltonian.

The Rashba orbital term has a mathematical form of an inhomogeneous magnetic field along y, with opposite directions for upper ($y > 0$) and lower ($y < 0$) sides of the wire. This yields an effective decrease of the magnetic field tilting angle with respect to the longitudinal direction, with Majorana regions expanding towards lower values of θ as shown in Fig. 8b. Remarkably, if the Rashba term is high enough we can have a Majorana phase with a magnetic field fully perpendicular to the nanowire ($\theta = 0$) in spite of the maximal orbital effect.

3.4 Calculating the Majorana state

Having determined the regions of the parameter space where to find the Majoranas, we can specifically calculate the detailed wave functions and probability distributions using the complex band structure method. In a

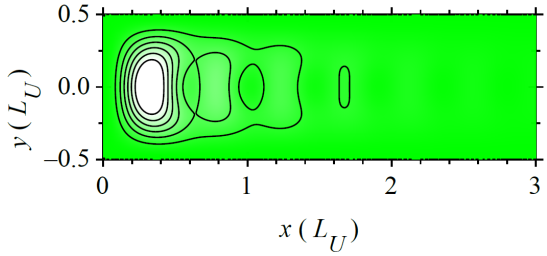

Fig. 9. Majorana density function in a semi-infinite nanowire for $\Delta_B = 10\,E_U$, $\phi = 0$, $\theta = 75°$, $\alpha = 3.14\,E_U L_U$, $\Delta_0 = 3\,E_U$ and typical InAs parameters $g = 15$, $m^* = 0.033$. Figure adapted from Ref. [41]

semi-infinite system there are is no hybridization between Majoranas on opposite ends, that can be important in finite size systems. In this sense, the phase transition is sharp and the end states are undisturbed by finite size effects. A large enough set of complex wave numbers and transverse wave functions $\{k, \Psi^{(k)}_{s_\sigma s_\tau}(y)\}$ are assumed to be known in advance. They can be obtained efficiently diagonalizing a sparse non-Hermitian matrix generalizing the method already discussed in the 1D case [41].

For a semininfinite wire with $x \geq 0$, the boundary condition at $x = 0$ reads

$$\sum_k C_k \, \Psi^{(k)}_{s_\sigma s_\tau}(y) = 0\,, \tag{32}$$

where the k values are such that $\Im(k) > 0$. This equation is recast in matrix form

$$\sum_k \mathcal{M}_{k'k}\, C_k = 0\,, \tag{33}$$

where

$$\mathcal{M}_{k'k} = \sum_{s_\sigma, s_\tau} \int dy\, \Psi^{(k')*}_{s_\sigma, s_\tau}(y) \Psi^{(k)}_{s_\sigma s_\tau}(y)\,. \tag{34}$$

Diagonalizing $\mathcal{M}$ with a large enough set of evanescent modes we have indeed obtained that it has a zero eigenvalue for each Majorana mode. In terms of the C_k amplitudes the corresponding wave function reads

$$\Psi(x, y, \eta_\sigma, \eta_\tau) = \sum_k C_k \, \Psi^{(k)}(x, y, \eta_\sigma, \eta_\tau)\,, \tag{35}$$

with $\Psi^{(k)}$ from Eq. (15). In Fig. 9 we can see the corresponding density function confirming the edge character of the mode as expected for a Majorana.

We stress that to obtain the Majorana wave function Eq. (35) we need to determine in advance the k's and $\Psi^{(k)}_{s_\sigma s_\tau}$'s for the corresponding edgeless nanowire. This can be done using the non-Hermitian matrix method presented in the preceding Sections. Once these results are known, the amplitudes C_k are obtained as the null eigenvectors of the diagonalization of $\mathcal{M}$, Eq. (33). The resulting Majorana wavefunction is then calculated as the linear superposition of the infinite nanowire modes with amplitudes C_k's. Null eigenvalues of matrix $\mathcal{M}$ are present only for the sets of parameters corresponding to the interior of a topological phase region of the phase diagram. This way, the assumption that $k = 0$ gap closings mark the position of phase boundaries is explicitly confirmed.

An important practical point is that finding a Majorana solution with a transverse resolution of various hundreds of points is not very demanding computationally with k analysis. On the other hand, the spatial resolution in x is arbitrarily high without any additional cost. Resolutions of 100×100 points seem to be on the computational limit for direct diagonalization in modern computers due to limits in memory size and computational power. With k-analysis the computational cost is of order $O(N_y^3) = O(N^3)$ to obtain k and $\Psi^{(k)}_{s_\sigma s_\tau}$, plus the cost of diagonalizing $\mathcal{M}$. The latter is $O(n_k^3)$ where n_k is the number of eigensolutions of the infinite wire considered. A relatively small $n_k < N_y$ can be used because only small $Im(k)$ are relevant for the Majorana wavefunction. Even for $n_k \approx N_y = N$, a very large number of k modes, the total cost is $O(N^3) + O(N^3) = 2O(N^3) = O(N^3)$. This is still much smaller than the $O(N^6)$ cost of direct diagonalization for a finite 2D-q1D nanowire. On the other hand, having the energy E as a parameter in the complex band structure approach, we do not obtain information of the full spectrum but only of the Majorana mode ($E = 0$) or on a restricted window of E's. Nevertheless in this particular problem this is not a big restriction because Majoranas are well isolated from non-topological above-gap states.

4 k-analysis in 3D-q1D

In a 3D-q1D wire the shape of the transverse section, in addition to simply the transverse size, becomes physically relevant. A particular class that has drawn much attention are core-shell nanowires, characterized by a repulsive core expelling electrons (quasiparticles) to the outer surface region. Often, these wires have prismatic shapes, with narrow quantum wells on the faceted outer shell of the wire [42–47]. In Ref. [48] it was suggested that prismatic core-shell wires can host Majorana end states when the prism edges behave in an effective way as q1D coupled wires. This leads to an interesting scenario, where multiple Majoranas may coexist, depending on the specific parameter set, on the same nanowire end. Braiding of such end Majoranas might then place prismatic nanowires as a suggestive platform for quantum computation.

The idea of the confinement along the prism edges of a prismatic wire originates in the geometric effects present in bent wires [49]. Indeed, it is known that the curved regions of a wire have a so-called geometric potential that may be strong enough to induce bound states at the bending. Such bound states have been also studied in planar polygons and piecewise linear wires [50,51]. Technically, extending 2D-q1D to 3D-q1D only requires generalizing the transverse wave functions of Eq. (15) to include now an extra transverse coordinate, $\Psi^{(k)}_{s_\sigma s_\tau}(y, z)$. The boundary

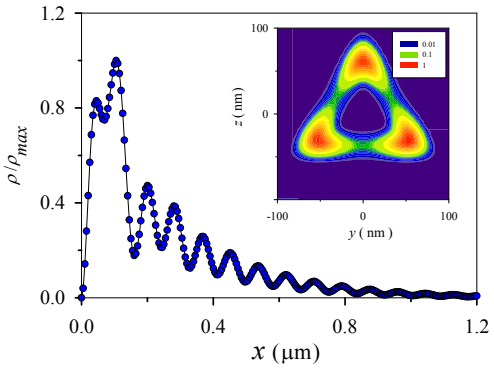

Fig. 10. Density of a zero-energy Majorana state in a triangular wire. Dots show the z evolution of the 1D density integrated in the transverse directions, while the inset shows in a color scale the transverse pattern for $z = 150$ nm, near the maximum of the integrated 1D density. Parameters: $R = 110$ nm, $t = 37.5$ nm, $\mu = 22.7$ meV, $\alpha = 50$ meVnm, $\Delta_0 = 0.5$ meV. From Ref. [48].

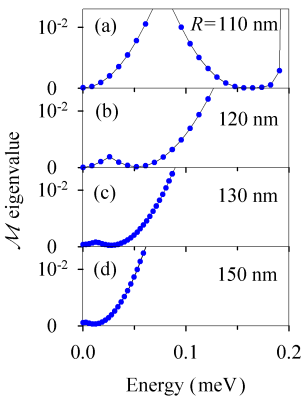

Fig. 11. Energy dependence of the lowest $\mathcal{M}$ eigenvalue in the semi-infinite triangular wire of Fig. 10. Null eigenvalues represent physical energies of states attached to $x = 0$ while decaying for increasing x. Panels (a) to (d) correspond to increasing shell radius and fixed $B = 0.73$ T. From Ref. [48].

condition for end states is still given by Eq. (33) but with a new $\mathcal{M}$ matrix

$$\mathcal{M}_{k'k} = \sum_{s_\sigma, s_\tau} \int dydz\, \Psi^{(k')*}_{s_\sigma, s_\tau}(y,z) \Psi^{(k)}_{s_\sigma s_\tau}(y,z)\,. \qquad (36)$$

In cases of multiple Majoranas, matrix $\mathcal{M}$ has degenerate null eigenvectors. Formally, the dimension of $\mathcal{M}$'s null space, known as kernel, is the number of Majoranas $n_\mathcal{M}$

$$\dim(\ker \mathcal{M}) = n_\mathcal{M}\,. \qquad (37)$$

The vanishing eigenvalues of $\mathcal{M}$ are clearly obtained for large enough sets of evanescent k's in practical applications.

In prismatic wires, the aspect ratio between the outer layer thickness t and the circumference radius R enclosing the outer polygon characterizes the coupling between the effective 1D prism edges. That is, a vanishing AR ($t/R \to 0$) represents well isolated wires while a sizeable AR, as obtained, e.g., by increasing t with a fixed R, corresponds to more strongly coupled wires. With a vanishing AR, the number of zero-energy Majorana pairs $n_\mathcal{M}$ (including both ends) coincides with the number of prism edges. The edge-edge coupling for finite AR lifts this zero-energy degeneracy. However, since electron-hole symmetry requires the eigenenergies to come in pairs with reversed signs this causes that with odd $n_\mathcal{M}$'s one state remains at precisely zero energy while the others come in pairs of small energies $\pm\epsilon_i$. In Ref. [48] these are called Majorana and pseudo-Majorana end states, respectively. With an even number of prism edges all $n_\mathcal{M}$ states become pseudo-Majoranas for a finite AR.

Figure 10 shows an end Majorana state in a triangular semi infinite wire ($x > 0$) with a sizeable AR. The density is localized on the prism edges and decays along the longitudinal distance. The hybridization leads to transverse patterns that change with the distance x from one to another prism edge. The density vanishes for $x = 0$, as required by the boundary condition Eq. (32), oscillates and decays exponentially for increasing x's. The AR dependence of the low energy Majorana-like states of the same triangular wire is displayed in Fig. 11. In this case $n_\mathcal{M} = 3$ and we observe a genuine zero-energy eigenvalue and a low-energy pseudo-Majorana pair at $\pm\epsilon$. Notice that, due to symmetry only the positive energies are shown in Fig. 11. As anticipated, the collapse to zero energy when the AR decreases in Fig. 11 in the sequence from panels a) to d) is quite clear.

5 NS junctions in 2D-q1D

In Secs. 2-4 we have described Majorana end states in semi-infinite nanowires. However, in actual experiments [2–8] Majorana nanowires are connected to normal leads in order to perform conductance measurements. In this section we return to the 2D-q1D geometry of Sec. 3 to study normal-superconductor (NS) junctions, i.e., junctions of a 2D-q1D normal lead and hybrid Majorana nanowire. One of the main advantages of wave number analysis, as compared to direct diagonalization methods, is the high spatial resolution at low computational cost. These high resolutions allow to calculate local currents at the NS junction and, more importantly, to relate the features of the current distribution with the precise value of the conductance in different conditions. The Hamiltonian of the Majorana nanowire, including orbital effects, was given in Eqs. (14) and (17). The main difference between NSN junctions and semi-infinite nanowires is that the junction equations are for interfaces, instead of hard edges [52].

We consider two infinite contacts separated by a junction as described in Fig. 12. The right contact is a superconductor while the left contact is a normal semiconductor. The junction is defined in an interface central region (C) between the leads. The solutions of each of the two

contacts are linear superpositions of the infinite homogeneous nanowire wavefunctions with well defined k's as in Sec. 3. Formally, both junctions sides are described with the same Hamiltonian Eq. (14) but with a zero superconductor coupling in the left (L) side of the junction, a finite value on the right (R) and a position-dependent value in the central (C) region. The asymptotic solutions read

$$\Psi(xy\eta_\sigma\eta_\tau) = \sum_{\alpha n_\alpha} d_{n_\alpha}^{(\alpha,c)} \exp\left[ik_{n_\alpha}^{(\alpha,c)}x\right]\phi_{n_\alpha}^{(\alpha,c)}(y\eta_\sigma\eta_\tau)\ , \tag{38}$$

where $\alpha = i, o$ labels the input (i) and output (o) modes for contact $c = L, C, R$.

Mathematically Eq. (38) has the same form of the eigensolutions of a semi-infinite nanowire. However, there are now ingoing and outgoing propagating modes of real wavenumber k and therefore the labelling is more involved. The 3-fold (α, n_α, c) labels are for the mode type (input or output), its ordering number and the contact (L,R), respectively. The output amplitudes $\{d_{n_o}^{(o,c)}\}$ determine the asymptotic solutions that can be arbitrarily extended in the leads since there the x-dependence is analytic. Non-propagating modes can be arbitrarily labeled also as output modes by convenience. As in a typical scattering problems, the algorithm has to yield the set of output amplitudes in terms of the input ones, for a given energy E, from

$$(\mathcal{H}_{BdG} - E)\,\Psi(xy\eta_\sigma\eta_\tau) = 0\ . \tag{39}$$

We extend the well known quantum-transmitting-boundary method of Ref. [53] to effectively perform the matching between the two sets of asymptotic solutions in a grid that contains the junction and small portions of the leads [52]. The wave function on the intermediate grid points are also unknowns although they play a rather auxiliary or instrumental role. The closed-system of linear equation reads

$$(\mathcal{H}_{BdG} - E)\,\Psi(xy\eta_\sigma\eta_\tau) = 0\ , \qquad (xy) \in C\ , \tag{40}$$

$$\Psi(xy\eta_\sigma\eta_\tau) - \sum_{n_o} d_{n_o}^{(o,c)} \exp\left[ik_{n_o}^{(o,c)}x\right]\phi_{n_o}^{(o,c)}(y\eta_\sigma\eta_\tau) = \sum_{n_i} d_{n_i}^{(i,c)} \exp\left[ik_{n_i}^{(i,c)}x\right]\phi_{n_i}^{(i,c)}(y\eta_\sigma\eta_\tau)\ , \quad (xy,c) \in L/R\ , \tag{41}$$

$$\sum_{\eta_\sigma\eta_\tau}\int dy\,\phi_{m_o}^{(o,c)}(y\eta_\sigma\eta_\tau)^*\,\Psi(x_c y\eta_\sigma\eta_\tau) - \sum_{n_o} d_{n_o}^{(o,c)} \exp\left[ik_{n_o}^{(o,c)}x_c\right]\mathcal{M}_{m_o n_o}^{(oc,oc)} = \sum_{n_i} d_{n_i}^{(i,c)} \exp\left[ik_{n_i}^{(i,c)}x_c\right]\mathcal{M}_{m_o n_i}^{(oc,ic)}\ , \qquad c \in L/R\ , \tag{42}$$

where x_c indicates the x coordinate of the grid points. Matrix $\mathcal{M}$ was already introduced in Sec. 3 and with the present labelling reads

$$\mathcal{M}_{m_\alpha n_\beta}^{(\alpha c,\beta c)} = \sum_{\eta_\sigma\eta_\tau}\int dy\,\phi_{m_\alpha}^{(\alpha,c)}(y\eta_\sigma\eta_\tau)^*\phi_{m_\beta}^{(\beta,c)}(y\eta_\sigma\eta_\tau)\ . \tag{43}$$

The low computational cost of this method is achieved at the expense of using energy as a parameter. Nevertheless, this is not a severe limitation for a transport problem because electrical conductance depends on reflection and transmission probabilities at a given energy. Wavenumber analysis yields an algorithm well suited to homogeneous systems separated by rather abrupt interfaces. The method requires locally homogenous regions connected by small interface regions (Fig. 12). In a broad sense, the algorithm is a generalization of the 1D matching method to include the transverse part of the wave function. An obvious limitation of the present k-analysis method is with cases where inhomogeneities or disorder are extended up to and including the asymptotic regions.

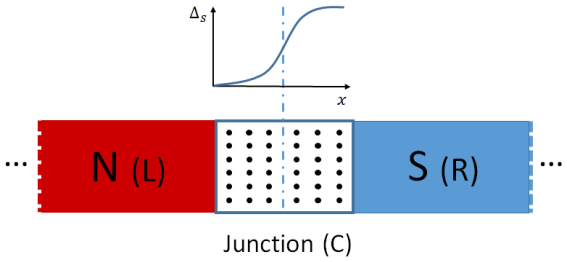

Fig. 12. Schematic of a 2D-q1D NS junction. The normal (N) and superconductor (S) at left (L) and right (R)) asymptotic regions are matched with a central (C) region. The junction is modelled with a grid where the superconductor coupling Δ_s increases with x creating an interface.

5.1 Spatial distribution of currents

NS junctions modelled with BdG equations do not conserve the number of electrons and holes due to the creation of Cooper pairs and the associated Andreev reflection, transforming one type of quasiparticle into the other. The reference state of the systems is a zero energy state containing an indeterminate number of Cooper pairs and new pairs end up hidden from the computation in the reference state. Nevertheless, the total BdG quasiparticle probability (not counting Cooper pairs) is conserved, with distributions of quasiparticle probability density $\rho_{qp}(x, y)$

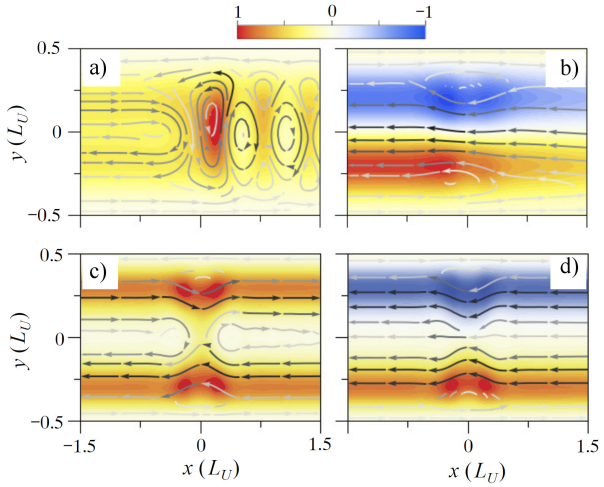

Fig. 13. Probability (color plot) and current (vector plot) for spatial distributions of quasi-particles (left) and charge (right). Panels a) and b) are obtained for a moderate non ideal magnetic field to show the resilence of the Majorana mode. That is, $\Delta_B = 12\,E_U$ and $(\theta,\phi) = (80^\text{o}, 10^\text{o})$. In this case non ideal, means that the magnetic field is not perfectly longitudinally oriented. Panels c) and d) are high magnetic field results, when edge modes are formed and the Majorana is split. They correspond to quasi-particle and charge spatial distributions for $\Delta_B = 30\,E_U$ and $(\theta,\phi) = (82^\text{o}, 0)$. Note that the maximum of the charge current centered on $y = 0$ is a Majorana signature as it prevails in this position no matter the non-ideal conditions provided the Majorana mode is not broken. Adapted from [52].

and current $\boldsymbol{\jmath}_{qp}(x,y)$ fulfilling the continuity equation

$$\frac{\partial \rho_{qp}}{\partial t} = -\nabla \cdot \boldsymbol{\jmath}_{qp}\ , \tag{44}$$

with

$$\rho_{qp}(x,y) = \Psi^*(x,y)\,\Psi(x,y)\ , \tag{45}$$
$$\boldsymbol{\jmath}_{qp}(x,y) = \Re\left[\,\Psi^*(x,y)\,\hat{\boldsymbol{v}}_{qp}\,\Psi(x,y)\,\right]\ , \tag{46}$$

where we defined the vector operator

$$\hat{\boldsymbol{v}}_{qp} = -i\frac{\hbar}{m}\nabla\,\tau_z + \frac{e}{mc}\boldsymbol{A} + \frac{\alpha}{\hbar}\left(\sigma_y \boldsymbol{u}_x - \sigma_x \boldsymbol{u}_y\right)\tau_z\ . \tag{47}$$

Expressions for the charge probability $\rho_c(x,y)$ and current $\boldsymbol{\jmath}_c(x,y)$ densities are easily obtained inserting $-e\tau_z$ in Eqs. (45) and (46) to take into account the charge difference between electron and holes

$$\rho_c(x,y) = -e\,\Psi^*(x,y)\,\tau_z\,\Psi(x,y)\ , \tag{48}$$
$$\boldsymbol{\jmath}_c(x,y) = -e\,\Re\left[\,\Psi^*(x,y)\,\hat{\boldsymbol{v}}_{qp}\tau_z\,\Psi(x,y)\,\right]\ . \tag{49}$$

Figure 13a and 13b show a representative result of the quasiparticle and charge currents in presence of a Majorana mode. The Majorana is attached to the junction interface that contains a potential barrier. In presence of vertical components of the magnetic field a big vortex of quasi-particle current is formed around the point of maximum probability of the Majorana mode. The incident electronic mode is attached to the top of the N side and it is reflected as a hole attached to the bottom N side, giving a U-shaped form in the current distribution (Fig. 13a).

As anticipated there is no local conservation of current in the junction; to allow for the electron to be reflected as a hole the junction behaves as a sink of electrons and as a source of holes. It is also remarkable that in presence of Majoranas the quasiparticle current is zero at the center of the nanowire ($y = 0$) because electron and hole particles propagate in opposite directions. Nevertheless, for the same reason the maximum charge current is also located at the center of the nanowire. This is true no matter the tilting of the magnetic field, provided the nanowire is kept within the borders of a Majorana phase. These borders can be exceeded by increasing the tilting, decreasing θ or increasing ϕ until the projection rule limit is exceeded. In 2D-q1D the projection rule Eq. 13 is only qualitatively fulfilled, with a critical angle ϕ_c where the gap is closed for the external branches. In Fig. 14 we can see the transverse distribution of currents for a cut of the nanowire, deep in the normal region. The maximum in quasi-particle current is lost abruptly when the critical angle is exceeded because an electronic channel is created when the gap is closed.

In high perpendicular magnetic fields the Majorana is lost due a loss in charge neutrality caused by the Rashba orbital effect discussed in Sec. 3. This term has the form of a non homogeneous magnetic field with opposite directions for $y > 0$ and $y < 0$. Large values of this term break Majorana neutrality splitting spatially the negative and positive charge terms of the wavefunction and reducing the imaginary part of the wavenumber, eventually yielding propagating channels for infinite values of the magnetic field. This loss is not signaled by any gap closing but it can be detected by the change in the current distribution as seen in Fig. 14b.

5.2 Conductance calculation

The output coefficients $d_{n_\alpha}^{(o,c)}$ obtained from the matching algorithm Eqs. (40)-(42) are all the required information to calculate the global conductance G. Specifically, with a given energy E it is

$$G(E) \equiv \frac{dI(E)}{dV} = \frac{e^2}{h}\left[N(E) - P_{ee}(E) + P_{eh}(E)\right]\ , \tag{50}$$

where

$$P_{ee}(E) = \sum_{n_o\,\eta_\sigma} \left|d_{n_o}^{(o,L)}\right|^2 \int dy\,\left|\phi_{n_o}^{(o,L)}(y,\eta_\sigma,\Uparrow)\right|^2\ , \tag{51}$$

$$P_{eh}(E) = \sum_{n_o\,\eta_\sigma} \left|d_{n_o}^{(o,L)}\right|^2 \int dy\,\left|\phi_{n_o}^{(o,L)}(y,\eta_\sigma,\Downarrow)\right|^2\ , \tag{52}$$

are the normal (electron-electron) and Andreev (electron-hole) reflection probabilities. In presence of a Majorana, perfect Andreev reflection of a single incident electron channel yields a conductance $2e^2/h$ of the NS junction. Of course, the spatial distribution of currents eventually

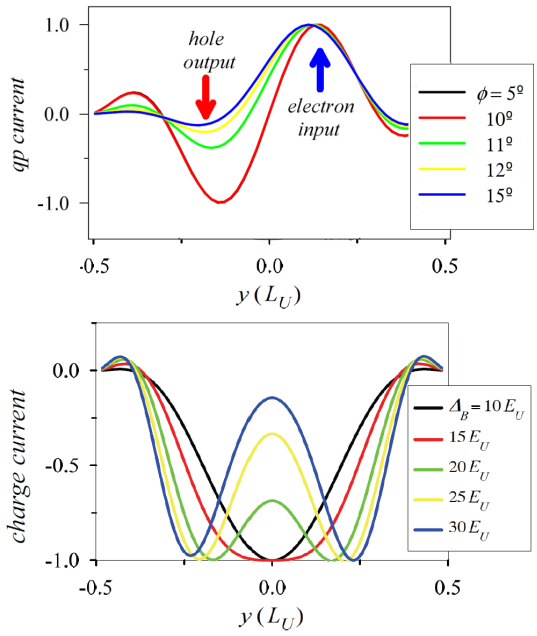

Fig. 14. Transverse cuts of the quasiparticle (a) and charge (b) currents in the normal lead. Panel a) uses the same parameters of Fig. 13a except of ϕ that is varied as specified. Once a critical angle is reached the gap is closed at the external branches and a pure electronic channel is opened trough the nanowire destroying the Majorana. Panel b) shows the evolution with Δ_B of a transverse cut in the charge current deep in the normal lead. For very strong magnetic fields the orbital effects split the Majorana in two charged halves. This is reflected in the transverse distribution with two maxima, one for each channel. Adapted from [52].

determines $G(E)$. As shown next, in presence of orbital effects large differences occur between the trivial and topological states of the superconductor due to the different transverse distribution of currents.

Summarizing, the calculation of conductance and distribution of currents of an NS junction requires; first, the eigensolutions of each of the leads as explained in the above Secs. 2 and 3; second, Eqs. (40), (41) and (42) are solved to obtain the asymptotic mode amplitudes and the wave function on a small grid around the junction. Note that the size of the grid makes the computation time of this last step small; in fact we need to consider only three rows of points in the longitudinal direction for a sharp junction. Finally, knowing the wave function and asymptotic amplitudes at energy E the density and current distributions are easily computed from Eqs. (45)-(49).

5.3 Magnetoconductance oscillations in NS junctions

The interplay of Andreev reflection and magnetic orbital effects was studied in Refs. [54–63]. In particular, Takagaki [55] studied the magnetoconductance of a 2D-q1D trivial NS junction. While those works considered a junction between a semiconductor and a true metallic superconductor, we assumed a hybrid topological superconductor [64]. Orbital effects were present only on the normal side of the junction due to the shielding of the metallic superconductor from the magnetic field. In that case, if high chemical potentials are considered increasing the magnetic field yields a reduction of the conductance in a stepwise manner due to the depopulation of the active bands of the semiconductor. However, the most interesting result is that for high enough fields magnetoconductance oscillations are observed in combination with the general stepwise trend of conductance reduction with increasing magnetic field.

Takagaki oscillations are seen in Fig. 15a and the reason behind them is the particular distribution of local currents at the junction, as shown in Fig. 15b. In presence of orbital effects the incident electron channel and the Andreev reflected hole channels are spatially separated, attached to different edges of the normal lead. In presence of orbital magnetic effects the two channels are connected trough multiple alternating electron-hole and hole-electron reflections as many half vortices occurring at the junction along the y direction. When an integer number of these reflections fit in the transverse width l_y a maximum in conductance arises; while for a half-integer number the conductance vanishes due to the loss of proper coupling between incident and reflected channels. We have reproduced Takagaki-like oscillations with a hybrid superconductor tuned to be in its trivial phase, instead of pure metallic superconductor. This means adding Rashba terms, not present in a metallic superconductor, and the coexistence of magnetic and superconductor couplings due to the superconductor hybrid nature.

To obtain full control of the topological phases, we assume independently tunable magnetic field strength and orientation on the two junction sides. The experimental feasibility and limitations of this control will be discussed later. A perpendicular magnetic field in the normal side (left) and a longitudinal one on the superconductor side (right) yields a proper interplay of orbital effects and Andreev reflection for the conductance oscillations. In an hybrid superconductor the external magnetic field is not shielded and therefore we change the orientation to avoid in it orbital effects. On the other hand, we can not drive the magnetic field strength to zero because it is needed to tune the nanowire from the trivial to the topological phase. In Figs. 15a and 15b the magnetic field in the superconductor side of the junction is maintained at a fixed strength to ensure the trivial phase of the superconductor.

Figures 16a and 16b show the local current distribution and the conductance as a function of the magnetic field; now for a hybrid superconductor in the topological phase. In this case conductance oscillations are totally suppressed at the two-incident-mode plateau. This happens because a single large vortex is formed at the junction, no matter the strength of the magnetic field, eliminating this way any transverse structure that may enhance or suppress Andreev reflection. Furthermore, in the topological phase only one channel is open to Andreev reflection, the other is reflected back as normal electron-electron scattering. This happens because there is only one topological channel as

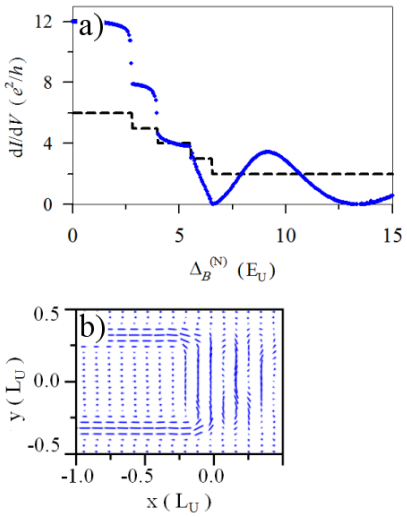

Fig. 15. a) Magnetoconductances of an NS junction with a trivial superconductor as a function of $\Delta_B^{(N)}$ for a fixed $\Delta_B^{(S)} = 6E_U$ (blue dots). The remaining parameters are $E = 0$, $\alpha^{(S)} = \alpha^{(N)} = 2E_U L_U$, $\Delta_0^{(S)} = 0.7E_U$, $\mu = 70E_U$. The ratio $\Delta_0^{(S)}/\mu$ is small enough (≈ 0.01) to ensure the validity of the so-called BTK regime. The smallest critical magnetic field of the hybrid wire is $\Delta_{B,4}^{(c)} \approx 7E_U$. The number of propagating modes in the N wire is given by the dashed line. b) Pattern of probability currents for the trivial phase of the superconductor lead. The parameters are the same of panel a). Adapted from Ref. [64].

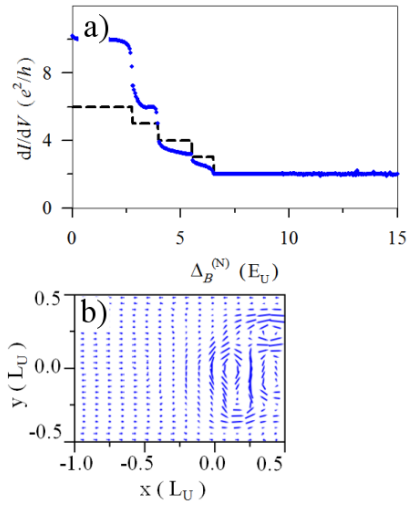

Fig. 16. a) Magnetoconductances of an NS junction with a topological superconductor as a function of $\Delta_B^{(N)}$ for a fixed $\Delta_B^{(S)} = 8E_U$ (blue dots). The remaining parameters are the same of Fig. 15. The number of propagating modes in the N wire is given by the dashed line. b) Pattern of probability currents for the topological phase of the superconductor lead. The parameters are the same of panel a). From Ref. [64].

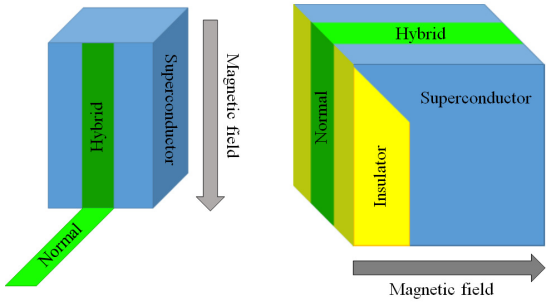

Fig. 17. Scheme of experiment proposal to achieve different field orientations in topological NS junctions. From Ref. [64].

the topological number of the superconductor may be only zero or one.

The above change of orientation of the magnetic field on the two junction sides may be effectively achieved bending the nanowire in presence of a uniform magnetic field. Figure 17 contains two simple proposals. Still, changes in magnetic field strength along the nanowire would require a finer control of the experiment, possibly using micromagnets, rather difficult to achieve. For this reason, Fig. 18 explores the visibility of Takagaki oscillations and their suppression in a model of constant magnetic field strength (but different orientation) on both sides of the junction. The main difficulty is now that increasing the magnetic field the system crosses the critical value between trivial and topological phases. Since the critical magnetic field Eq. (23) is affected by the width of the nanowire through the eigenenergies $\epsilon_n = n^2\pi^2\hbar^2/2ml_y^2$, it is still possible to observe conductance oscillations tuning l_y. Indeed, Fig. 18 shows that for different widths it is possible to see Takagaki oscillations, supress them or see the change from one regime to the other.

6 Conductance oscillations with chiral Majoranas

6.1 Topological insulator two layer model

This section discusses junctions between a topological insulator and a superconducting region holding chiral Majorana modes. Chiral Majorana modes are 1D propagating states with real wavenumber k propagating along the edges of a 2D-q1D slab with a well defined sense of rotation, either clockwise or anticlockwise. They are intrinsically different to the localized Majorana end states discussed above and they can be obtained with topological insulators based on quantum anomalous Hall (QAH) materials [22–28].

We consider a slab made of a topological insulator of a certain thickness modeled as a double-layer QAH strip with a different superconducting strength in each layer and an intrinsic magnetization. The Hamiltonian reads

$$\begin{aligned}\mathcal{H} = &\left[\, m_0 + m_1 \left(p_x^2 + p_y^2\right) \right] \tau_z \lambda_x + \Delta_Z \sigma_z \\ &- \frac{\alpha}{\hbar} \left(p_x \sigma_y - p_y \sigma_x\right) \tau_z \lambda_z \\ &+ \Delta_p \tau_x + \Delta_m \tau_x \lambda_z \,, \end{aligned} \tag{53}$$

where the superconductivity parameters $\Delta_{p,m}$ are written by convenience as the half-sum/half-difference of the

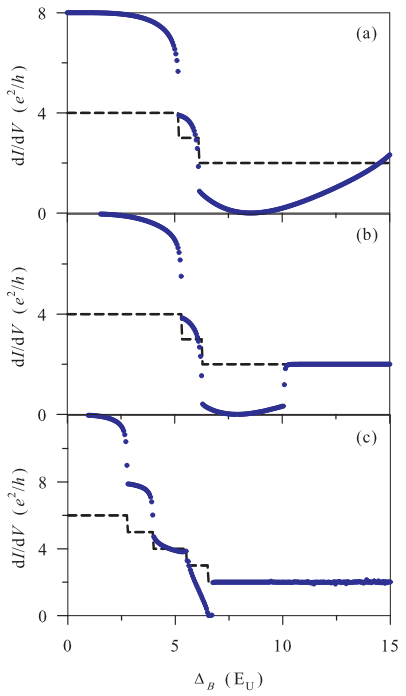

Fig. 18. Conductance at zero energy as a function of the perpendicular magnetic field at the normal (left) side of the junction $\Delta_B^{(L)}$. In this case the magnetic field strength is maintained equal at both side of the junction $\Delta_B^{(L)} = \Delta_B^{(R)}$ to better represent the experiments depicted in Fig. 17. Note that the orientation of the field at both sides of the junction continues to be different. The rest of the parameters are the Rashba coupling strength $\alpha = 2.0 E_U L_U$, the superconductor gap $\Delta_o = 0.7 E_U$ and the chemical potential $\mu = 70 E_U$. The critical magnetic field in the superconductor side of the junction is controlled changing the transverse width of the nanowire L_y where a) $L_y = 0.7 L_U$, b) $L_y = 0.73 L_U$, c) $L_y = 1.0 L_U$. From Ref. [64].

corresponding couplings of the two layers, $\Delta_{p,m} \equiv (\Delta_1 \pm \Delta_2)/2$. As usual in this review, Pauli matrices are used for the two-valued variables representing usual spin $\boldsymbol{\sigma}$ and electron-hole isospin $\boldsymbol{\tau}$. Besides, we now add a layer index pseudo-spin $\boldsymbol{\lambda}$ for top and bottom layers of the topological insulator. In this case, the Nambu spinor representation is extended to include the field operators of the top (t) and bottom (b) layers,

$$\left[(\Psi^t_{k\uparrow}, \Psi^t_{k\downarrow}, \Psi^{t\dagger}_{-k\downarrow}, -\Psi^{t\dagger}_{-k\uparrow}), (\Psi^b_{k\uparrow}, \Psi^b_{k\downarrow}, \Psi^{b\dagger}_{-k\downarrow}, -\Psi^{b\dagger}_{-k\uparrow})\right]^T .$$

The scattering problem at the junction was solved in Ref. [65] with the method of the preceding section. As in Eq. (38), the wave function for each portion of the strip with constant parameters is expanded in its corresponding complex band structure

$$\Psi(xy\eta_\sigma\eta_\tau\eta_\lambda) = \sum_{\alpha n_\alpha} d^{(\alpha,c)}_{n_\alpha} e^{ik^{(\alpha,c)}_{n_\alpha}(x-x_c)} \phi^{(\alpha,c)}_{n_\alpha}(y\eta_\sigma\eta_\tau\eta_\lambda) \, . \tag{54}$$

The device has two NS junctions separating the superconducting region from the left and right normal contacts

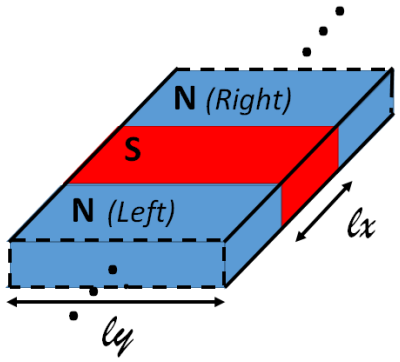

Fig. 19. Sketch of the NSN double junction of QAH material displaying conductance oscillations in the limit of narrow widths $\ell_y < 5$ μm.

(see a sketch in Fig. 19). The phase $e^{-ik^{(\alpha,c)}_{n_\alpha} x_c}$ has been added to Eq. (54), in comparison with the above single NS junction, for numerical convenience. The method of Ref. [65] requires just a minimal grid of $N_x = 3$ points centered on each interface. Of course, k and Φ_k must be known in advance in a large set, as explained in Sec. 3.

Half quantum conductance $0.5e^2/h$ due to a chiral Majorana has been measured in QAH strips of 2×1 mm with a small central part of the strip ($\ell_x \approx 0.8$ mm) proximity coupled with a metallic superconductor [22]. We discuss below the prediction that with narrower strips of $\ell_y < 5$ μm characteristic conductance oscillations with applied bias or with system length ℓ_x are present.

The two terminal conductance is calculated as

$$G(E) = \frac{e^2}{h} \left[T_N(E) + R_A(E) \right] \, , \tag{55}$$

where T_N is the normal (electron-electron) transmission probability and R_A is the Andreev (electron-hole) reflection probability. The energy E is related to the bias V by $E = eV/2$. Transmission and reflection probabilities are obtained from the scattering amplitudes of the output modes,

$$T_N(E) = \sum_{n_o \eta_\sigma \eta_\lambda} \left| d^{(o,R)}_{n_o} \right|^2 \int dy \left| \phi^{(o,R)}_{n_o}(y, \eta_\sigma, \Uparrow, \eta_\lambda) \right|^2 , \tag{56}$$

$$R_A(E) = \sum_{n_o \eta_\sigma, \eta_\lambda} \left| d^{(o,L)}_{n_o} \right|^2 \int dy \left| \phi^{(o,L)}_{n_o}(y, \eta_\sigma, \Downarrow, \eta_\lambda) \right|^2 . \tag{57}$$

We consider a symmetrical bias drop in the two terminals, with a grounded superconductor [24]. In Refs. [66–69] quasiparticle-reversal transmission and its dependence with the superconductor chemical potential has been discussed. Interferometry with Majorana beam splitters, where quasiparticles are constrained to follow different paths, was considered in [70–72].

6.2 Conductace oscillations with energy

In Fig. 20a we can see the bias-dependent conductance $G(E)$ for a wide slab. For small bias, the well known result

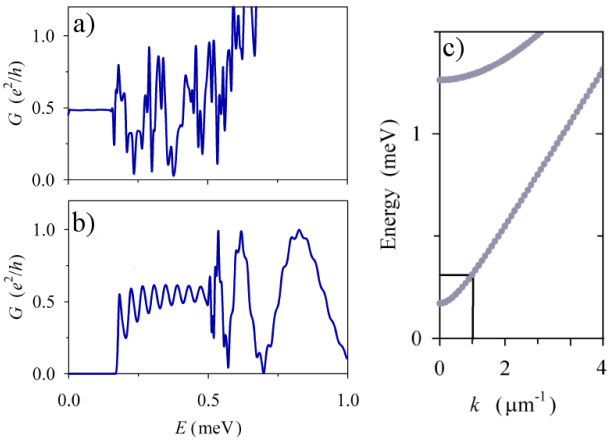

Fig. 20. Panels a) and b): Conductance as a function of the energy/bias for $\ell_y = 5$ μm (a) and 1 μm (b). The two panels are for $\ell_x = 20$ μm and $\Delta_Z = 1.5$ meV. c) Energy bands for the case $\ell_y = 1$ μm. The rest of parameters for all three panels are $\alpha = 0.26\,\text{meV}\mu\text{m}$, $m_0 = 1\,\text{meV}$, $m_1 = 10^{-3}\,m_U^{-1}$, $\Delta_1 = 1\,\text{meV}$ and $\Delta_2 = 0.1\,\text{meV}$ mimicking the experimental values of [22] with Cr doped and V doped $(Bi,Sb)_2Se_3$ or $(Bi,Sb)_2Te_3$. It is assumed a unit system set by 1 meV, the mass unit m_U is set from the condition $\hbar \equiv m_U^{1/2}\text{meV}^{1/2}\mu\text{m}$, yielding $m_U = 7.6 \times 10^{-5} m_e$, where m_e is the bare electron mass. Adapted from [65].

that a chiral Majorana is characterized by a half quantum conductance is clearly seen. However, for a narrower slab we can see conspicuous oscillations around that value in Fig. 20b. The reason is that in the ideal wide slab scenario an incident electron is reflected with a 0.5 probability in the first superconductor interface and it is transmitted into the superconductor also with a 0.5 probability. In fact, the electron is Andreev reflected as a hole with $R_{eh} = 0.25$ and as a normal electron with $R_{ee} = 0.25$. Transmission splits also in a similar way, with equal transmissions into electron and hole, $T_{ee} = 0.25$ and $T_{eh} = 0.25$. This peculiar share of probabilities is necessary to fulfil charge neutrality of the Majorana mode.

In the ideal case, the second interface is transparent to the transmission of the Majorana channel into the right contact. However, if the nanowire is narrow the Majorana modes of the two transverse edges are coupled; they are actually becoming coupled quasi Majoranas. In this new scenario, the second interface is not totally transparent and some backscattering happens. The backscattered channel interferes with the reflected ones on the first interface in a constructive or destructive way (see Fig. 20b) depending on the length ℓ_x and energy E.

Note that the backscattered channel will be characterized by a particular wavenumber that with an integer or semi-integer number of wavelengths will exactly fit in the length ℓ_x. The interference will be constructive or destructive depending on the relation of the wavenumber and the length of the superconductor region. On the other hand, the quasi-Majorana mode lies in a topological band with a linear (or almost linear) dispersion relation $E \approx c\hbar k$ (as shown inFig. 20c). Therefore, with a constant superconductor length (a reasonable assumption in experiment) the energy or the bias will affect the ratio yielding the oscillations shown in Fig. 20b.

The separation between successive conductance maxima of $G(E)$ is related to the speed c of the chiral Majorana mode. Considering that a conductance maximum requires an integer number of half wavelengths to fit in distance ℓ_x, the velocity of the dispersion relation is $c = \ell_x \Delta E/\pi$, where ΔE is the separation of two successive maxima. This reproduces $c \approx 0.26\,\text{meV}\mu\text{m}/\hbar$ for the results of Fig. 20b. A key point here is to realize that a transverse effect due to the finite size of the strip leads to a longitudinal effect, eventually affecting the conductance of narrow strips. This may be a large effect, easily reaching 40-50 % conductance variations for energies near the lowest band energies in Fig. 20b. We finally stress that the suggested measurement of the chiral Majorana speed c from the oscillation pattern is equivalent to determining the effective spin-orbit coupling α since $\alpha \approx \hbar c$.

7 Optical absorption

Majorana zero energy modes are chargeless and spinless and these attributes also make them very difficult to detect. Experiments have focused mainly on the electrical conductance properties of Majoranas, but it has proved hard to arrive at fully conclusive results. In this Section, last one before the Conclusions, we review our recent works suggesting Majorana detection by their optical absorption properties. Like in previous Sections we stress key aspects of both calculation techniques and results. The Section is divided into two parts: first part discusses optical properties of hybrid semiconductor-superconductor nanowires with wire-end Majorana modes, while second is on optical properties of proximity coupled topological insulator with chiral edge Majorana modes.

7.1 Optical absorption of wire-end Majoranas

This section discusses calculations of the optical absorption of a 2D-q1D nanowire in longitudinal magnetic field [73,74], with the Hamiltonian of Eq. (14) of Sec. 3. The first step is to numerically diagonalize the Hamiltonian for a finite nanowire. This is a computer costly operation since in this case a large energy window of the spectrum is needed to calculate the absorption/emission cross section. The diagonalization can be performed either using an xy spatial grid or with a mixed grid-basis approach. In the latter, only the x coordinate is discretized while the transverse degree of freedom is described with a basis of square well eigenstates. The mixed method is preferred for narrow wires since it allows describing rather abrupt borders due to the finer longitudinal mesh.

We calculate the dipole absorption cross section, in the limit of weak EM field,

$$\sigma(\omega) \approx \sum_{k,s} \frac{|\langle k|\boldsymbol{p}\cdot\hat{e}|s\rangle|^2}{\omega_{ks}}\,\delta(\omega-\omega_{ks})\,f_s\,(1-f_k)\,, \qquad (58)$$

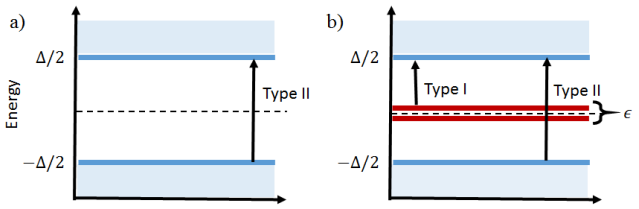

Fig. 21. Schematic band structure for a nanowire in a) the trivial phase and b) the topological phase. Transitions of types I and II are indicated. Majorana near-zero modes are shown in red, with a finite-size energy splitting ϵ.

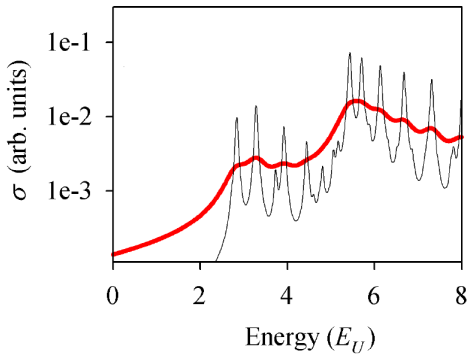

Fig. 22. Absorption cross section for y-polarized light of a hybrid nanowire in the topological phase. The nanowire parameters are $\Delta_B = 10E_U$, $\Delta_S = 3\,E_U$, $\alpha = 3.1\,E_U L_U$, $\mu = 20\,E_U$, $L_y = 0.5\,L_U$ and $L_x = 30\,L_U$. Dirac deltas of Eq. (58) are smoothened into Lorentzians of width Γ, mimicking the experimental resolution. Thick lines are smoothened absorptions obtained with larger Γ than thin lines; only the latter are able to resolve individual peaks. Figure adapted from [73].

where $f_{s,k}$ are Fermi functions for the occupation of levels s, k with temperature T while $\hat{e}$ is a unitary vector giving the polarization direction of the EM field. Equation (58) relates the absorption with the electronic transitions between levels.

Figure 21 show schematically the band structure of a typical hybrid nanowire in the trivial and topological phases. Electromagnetic absorption is related to electron jumps from occupied low energy states to empty high energy ones. In the trivial phase, only type II transitions between states above the gap are possible, with $\hbar\omega > \Delta_0$. In contrast, the topological regime reduces further the lower absorption limit due to the Majorana mode located near zero energy and its associated transitions of type I, $\hbar\omega > \Delta_0/2$.

In Fig. 22 the dipole absorption of a topological nanowire with y-polarized light is shown. When the Majorana mode is present, the absorption shows a double plateau. The first one starts at half the energy gap while the second starts at the energy of the full gap. The two-plateau behaviour is obtained only in presence of Majoranas and with y-polarized light; x-polarized light does not allow to clearly distinguish the two absorption plateaus [73,74].

Transitions between Majorana states in Fig. 21b are forbidden by a selection rule with the dipole operator in particle-hole symmetric systems. The symmetry operator $\Theta \equiv -\sigma_y\tau_y\mathcal{K}$, where $\mathcal{K}$ is the conjugation operator, relates a $|\Psi_E\rangle$ eigenstate with energy E with its pair-conjugate $\Theta|\Psi_E\rangle$ with energy $-E$. The dipole matrix element with such particle-hole conjugate states vanishes

$$\begin{aligned}\langle\Psi_E|\boldsymbol{p}\,|\Psi_{-E}\rangle &= \langle\Psi_E|\boldsymbol{p}\,\Theta|\Psi_E\rangle = \\ &= -i\hbar\int_{-\infty}^{+\infty}(\psi^*_{\uparrow\Uparrow},\psi^*_{\uparrow\Downarrow},\psi^*_{\downarrow\Uparrow},\psi^*_{\downarrow\Downarrow})\,\nabla\begin{pmatrix}\psi^*_{\downarrow\Downarrow}\\ -\psi^*_{\downarrow\Uparrow}\\ -\psi^*_{\uparrow\Downarrow}\\ \psi^*_{\uparrow\Uparrow}\end{pmatrix}d^2r \\ &= -i\hbar\int_{-\infty}^{+\infty}\nabla\left(\psi^*_{\uparrow\Uparrow}\psi^*_{\downarrow\Downarrow}-\psi^*_{\uparrow\Downarrow}\psi^*_{\downarrow\Uparrow}\right)d^2r = 0\,. \qquad (59)\end{aligned}$$

That is, a selection rule forbids dipole transitions from $|\Psi_E\rangle$ to $|\Psi_{-E}\rangle$. This result makes sense from the point of view of the topological protection; the Majorana modes must be protected from each other by their topological nature.

7.2 Optical absorption of chiral Majoranas

In this Section we consider a two layer hybrid QAH insulator like the one described in Sec. 6. With a strip of only a few microns width an xy grid diagonalization is still a viable choice [75]. For square or rectangular strips with similar longitudinal and transverse dimensions it is irrelevant to use x or y polarized light. In Ref. [75] we computed the circular dichroism at a given frequency $\mathcal{S}_{CD}(\omega)$. The circular dichroism is defined as the difference between the absorptions for the two circular polarizations,

$$\mathcal{S}_{CD}(\omega) = \mathcal{S}_+(\omega) - \mathcal{S}_-(\omega)\,, \qquad (60)$$

where, the optical absorption cross section for right $(+)$ and left $(-)$ circularly-polarized light are

$$\mathcal{S}_\pm(\omega) = 4m_1^2\sum_{k>0,s<0}\frac{1}{\omega_{ks}}\left|\langle k|p_x \pm ip_y|s\rangle\right|^2\delta(\omega-\omega_{ks})\,. \qquad (61)$$

Note that $\hbar\omega_{ks} = \varepsilon_k - \varepsilon_s$ is the energy difference between the empty and filled states. Obviously, in absence of any chirality preference in the device $\mathcal{S}_{CD}$ will vanish.

When the eigenenergies of the finite strip are plotted as a function of the angular momentum z-component, $\langle J_z\rangle$, the quasi-Majorana states arrange on a line equally spaced in energy (see Fig. 23). In this case the lower energy transitions are between states of the same topological band. From a topological point of view this is possible because they are not perfect but quasi-Majorana states. The selection rules for transitions between the negative n-th state to the positive m-th state $(-n \to m)$ are:

a) transitions between conjugate states $-n \to n$ are forbidden by particle-hole symmetry,
b) n even to m odd transitions (or vice versa) are forbidden because of destructive interference along the nanostructure perimeter with the excitation operator.

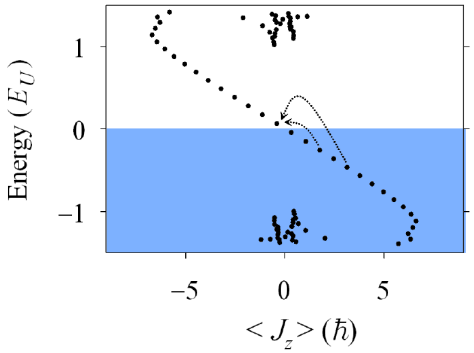

Fig. 23. Eigenvalues as a function of $\langle J_z \rangle$ for a topological insulator of dimensions $L_x = 2L_y = 20\,L_U$. The topological insulator is proximity coupled with a different superconductor in each layer with pairing energies $\Delta_1 = \Delta_2/3 = E_U$. The rest of the parameters are $\Delta_B = 2E_U$, $m_0 = 0$, $\mu = 0$, $\alpha = E_U L_U$. The device is in the topological phase holding a chiral Majorana mode. The blue-shaded region corresponds to the occupied states while the white region is for the empty ones. The arrows show the two lowest allowed transitions to the first unoccupied state. Figure adapted from [75].

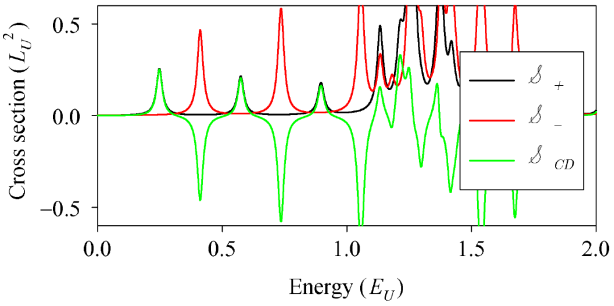

Fig. 24. Absorption cross sections $\mathcal{S}_+$, $\mathcal{S}_-$ and $\mathcal{S}_{CD}$ for a square of $L_x = L_y = 20\,L_U$. The rest of the parameters are the same of Fig. 23. Adapted from [75].

Note, too, that these selection rules are valid for square or rectangular strips where J_z is not a good quantum number and the states amplitude is expected to spread to several neighbouring values. For a disc, where J_z is a good symmetry, only the transition $-1 \to 1$ is possible due to angular momentum conservation but particle hole symmetry forbids this transition. Therefore, no optically induced transitions are possible in disk geometries. This is a particular key result that distinguishes chiral from non-chiral Majoranas. The fact that chiral Majoranas attach to all four edges of an insulator strip makes absorption properties depend on the geometry, with corners playing a nontrivial role on the optical absorption by chiral edge states.

Figure 24 shows the absorption spectrum for a square geometry. The first peaks of the circular dichroism alternate sign and the most conspicuous feature is their regular energy spacing. This spacing is explained by the above selection rules that restrict the possible transitions from the negative n-th state to the positive m-th. The peaks correspond to jumps of $3, 5, 7, \ldots$ steps (see arrows in Fig. 23a).

8 Conclusions

Complex band structure techniques allow a direct and specific modelling of topological 1D and q1D wires hosting low dimensional Majorana modes; either at their ends in hybrid semiconducting wires or on their lateral edges in strips of hybrid QAH insulators. The topological phase boundaries are efficiently determined from the condition of a vanishing $k = 0$ eigenenergy. Wire junctions characterized by constant parameter sets in sequential regions along the longitudinal wire direction are described in a two-step approach: first a large set of complex wavenumbers and transverse wavefunction for each region is calculated, second an effective matching is achieved by a minimal grid discretization around each interface. This approach allows large spatial resolutions, as required for a proper characterization of the density and current distributions.

The main physical results discussed in this work are:

a) In the limit of a 1D hybrid semiconductor wire the dependence of the Majorana phase boundary is set by a *projection rule*, in addition to the known field strength rule. This projection rule is obtained in Sec. 2 analysing the existence of a solution of the boundary condition on the wire end in terms of the wave numbers and wave functions of the corresponding homogeneous wire.

b) In 2D-q1D hybrid semiconductor wires, orbital effects when the field has a perpendicular component are very relevant and lead to critical polar angles. For large fields these critical polar angles are analytical. This result is obtained in Sec. 3. The bulk to edge correspondence principle relates the topological properties of the finite (or semiinfinite) nanowire with the infinite one. In an infinite nanowire the Majorana phase transition implies the closing an reopening of the gap at $k = 0$. We introduced a continuity measure $\mathcal{F}$ such that the condition $\mathcal{F} = 0$ yields the Majorana phase boundaries in a computer efficient way without carrying out a full diagonalization of the Hamiltonian matrix.

c) In prismatic 3D-q1D hybrid wires of core-shell type, analyzed in Sec. 4, Majorana end modes along the prism edges are formed. Majorana modes on different prism edges are coupled, depending on the aspect ratio between radius and width of core and shell, respectively. We use an extension to 3D of the method presented in Sec. 3 to calculate Majorana wave functions in 2D-q1D.

d) Topological NS junctions of hybrid semiconductor wires show characteristic patterns of density and currents when a Majorana mode is found at the junction interface. In presence of a vertical field component, Takagaki conductance oscillations are seen in the trivial phase but not in the topological phase of a Majorana mode. This result is obtained in Sec. 5 where we extend the methods of Sec. 4 to an NS junction. This amounts to substitute the set of equations obtained

from the edge condition by a set equations matching the solutions for the leads on both sides of the junction.

e) In Sec. 6 we find that NSN topological junctions of 2D-q1D hybrid strips with chiral Majoranas show conspicuous conductance oscillations with bias, for strip transverse widths lower than a few microns. This is obtained applying the methods of Sec. 5 to a device holding chiral Majoranas instead of the end-localized ones. The number of equations is doubled to solve simultaneously the two sequential NS junctions. The obtained oscillations are due to backscattering of the chiral Majoranas between the two interfaces of the NSN double junction. Measuring the oscillation period yields the speed of the chiral Majoranas.

f) Finally, in Sec. 7 we compute the optical absorption spectrum of 2D finite wires hosting end-localized and chiral Majoranas. Knowledge of a large set of eigenmodes is required in order to calculate the absorption spectrum; therefore, in this particular case the diagonalization of the Hamiltonian for a finite nanowire is needed. The absorption spectrum shows characteristic features in presence of Majorana modes: wire-end Majoranas yield an absorption plateau at half the energy gap for y-polarized electromagnetic field; chiral Majoranas yield circular dichroism with equally spaced peaks of alternating signs.

We acknowledge support from MINECO (Spain), grant MAT2017-82639.

Both authors contributed equally to all aspects of the work.

References

1. E. Majorana, Nuovo Cimento **14**, 171 (1937)
2. V. Mourik, K. Zuo, S. Frolov, et al., Science **336**, 1003 (2012)
3. M. T. Deng, C. L. Yu, G. Y. Huang, et al., Nano Letters **12**, 12, 6414 (2012)
4. L. P. Rokhinson, X. Liu, J. K. Furdyna, Nature Physics **8**, 795 (2012)
5. A. Das, Y. Ronen, Y. Most, et al., Nat Phys **8**, 12, 887 (2012)
6. A. D. K. Finck, D. J. Van Harlingen, P. K. Mohseni, et al., Phys. Rev. Lett. **110**, 126406 (2013)
7. Ö. Gül, H. Zhang, J. D. S. Bommer, et al., Nature Nanotechnology **13**, 3, 192 (2018)
8. H. Zhang, C.-X. Liu, S. Gazibegovic, et al., Nature **556**, 74 EP (2018)
9. J. Alicea, Rep. Prog. Phys. **75**, 076501 (2012)
10. C. W. J. Beenakker, Annual Review of Condensed Matter Physics **4**, 1, 113 (2013)
11. M. Franz, Nat Nano **8**, 3, 149 (2013)
12. T. D. Stanescu, S. Tewari, Journal of Physics: Condensed Matter **25**, 23, 233201 (2013)
13. R. Aguado, La Rivista del Nuovo Cimento **40**, 11, 523 (2017)
14. R. M. Lutchyn, E. P. A. M. Bakkers, L. P. Kouwenhoven, et al., Nature Reviews Materials **3**, 5, 52 (2018)
15. P. F. Bagwell, Phys. Rev. B **41**, 10354 (1990)
16. J. Barbosa, P. Butcher, Superlattices and Microstructures **22**, 3, 325 (1997)
17. J. K. Tomfohr, O. F. Sankey, Phys. Rev. B **65**, 245105 (2002)
18. L. Serra, Phys. Rev. B **87**, 075440 (2013)
19. M. Z. Hasan, C. L. Kane, Rev. Mod. Phys. **82**, 3045 (2010)
20. X.-L. Qi, S.-C. Zhang, Rev. Mod. Phys. **83**, 1057 (2011)
21. C.-K. Chiu, J. C. Y. Teo, A. P. Schnyder, et al., Rev. Mod. Phys. **88**, 035005 (2016)
22. Q. L. He, L. Pan, A. L. Stern, et al., Science **357**, 6348, 294 (2017)
23. X.-L. Qi, T. L. Hughes, S.-C. Zhang, Phys. Rev. B **82**, 184516 (2010)
24. S. B. Chung, X.-L. Qi, J. Maciejko, et al., Phys. Rev. B **83**, 100512 (2011)
25. J. Wang, B. Lian, H. Zhang, et al., Phys. Rev. Lett. **111**, 086803 (2013)
26. J. Wang, B. Lian, S.-C. Zhang, Phys. Rev. B **89**, 085106 (2014)
27. J. Wang, Q. Zhou, B. Lian, et al., Phys. Rev. B **92**, 064520 (2015)
28. B. Lian, J. Wang, S.-C. Zhang, Phys. Rev. B **93**, 161401 (2016)
29. B. Lian, X.-Q. Sun, A. Vaezi, et al., Proceedings of the National Academy of Sciences **115**, 43, 10938 (2018)
30. B. Lian, J. Wang, X.-Q. Sun, et al., Phys. Rev. B **97**, 125408 (2018)
31. "HSL (2013). A collection of Fortran codes for large scale scientific computation. http://www.hsl.rl.ac.uk"
32. L. Serra, D. Sánchez, R. López, Phys. Rev. B **76**, 045339 (2007)
33. R. B. Lehoucq, D. C. Sorensen, C. Yang, *ARPACK Users Guide: Solution of Large-Scale Eigenvalue Problems with Implicitly Restarted Arnoldi Methods* (Philadelphia: SIAM. ISBN 978-0-89871-407-4, 1998)
34. F. Tisseur, K. Meerbergen, SIAM Review **43**, 2, 235 (2001)
35. Y. Oreg, G. Refael, F. von Oppen, Phys. Rev. Lett. **105**, 177002 (2010)
36. J. Osca, D. Ruiz, L. Serra, Phys. Rev. B **89**, 245405 (2014)
37. P. San-Jose, E. Prada, R. Aguado, Phys. Rev. Lett. **112**, 137001 (2014)
38. R. M. Lutchyn, T. D. Stanescu, S. Das Sarma, Phys. Rev. Lett. **106**, 127001 (2011)
39. R. M. Lutchyn, M. P. A. Fisher, Phys. Rev. B **84**, 214528 (2011)
40. J. S. Lim, L. Serra, R. Lopez, et al., Phys. Rev. B **86**, 121103 (2012)
41. J. Osca, L. Serra, Phys. Rev. B **91**, 235417 (2015)
42. M. Hu, X. Zhang, K. P. Giapis, et al., Phys. Rev. B **84**, 085442 (2011)
43. B. M. Wong, F. Léonard, Q. Li, et al., Nano Letters **11**, 8, 3074 (2011)
44. C. Blömers, T. Rieger, P. Zellekens, et al., Nanotechnology **24**, 3, 035203 (2013)
45. F. Qian, M. Brewster, S. K. Lim, et al., Nano Letters **12**, 6, 3344 (2012)
46. M. Heurlin, T. Stankevič, S. Mickevičius, et al., Nano Letters **15**, 4, 2462 (2015)
47. X. Yuan, P. Caroff, F. Wang, et al., Advanced Functional Materials **25**, 33, 5300 (2015)
48. A. Manolescu, A. Sitek, J. Osca, et al., Phys. Rev. B **96**, 125435 (2017)

49. J. T. Londergan, J. P. Carini, D. P. Murdock, *Binding and Scattering in Two-Dimensional Systems. Applications to Quantum Wires, Waveguides and Photonic Crystals* (Springer, 1999)
50. C. Estarellas, L. Serra, Superlattices and Microstructures **83**, 184 (2015)
51. C. Estarellas, L. Serra, Phys. Rev. E **93**, 032105 (2016)
52. J. Osca, L. Serra, Eur. Phys. J. B **90**, 2, 28 (2017)
53. C. S. Lent, D. J. Kirkner, Journal of Applied Physics **67**, 10, 6353 (1990)
54. C. W. J. Beenakker, Phys. Rev. B **46**, 12841 (1992)
55. Y. Takagaki, Phys. Rev. B **57**, 4009 (1998)
56. Y. Asano, Phys. Rev. B **61**, 1732 (2000)
57. H. Hoppe, U. Zülicke, G. Schön, Phys. Rev. Lett. **84**, 1804 (2000)
58. F. Giazotto, M. Governale, U. Zülicke, et al., Phys. Rev. B **72**, 054518 (2005)
59. J. Eroms, D. Weiss, J. D. Boeck, et al., Phys. Rev. Lett. **95**, 107001 (2005)
60. N. M. Chtchelkatchev, I. S. Burmistrov, Phys. Rev. B **75**, 214510 (2007)
61. P. Rakyta, A. Kormányos, Z. Kaufmann, et al., Phys. Rev. B **76**, 064516 (2007)
62. I. M. Khaymovich, N. M. Chtchelkatchev, I. A. Shereshevskii, et al., EPL (Europhysics Letters) **91**, 1, 17005 (2010)
63. P. Carmier, Phys. Rev. B **88**, 165415 (2013)
64. J. Osca, L. Serra, Phys. Status Solidi B **1521-3951** (2017)
65. J. Osca, L. Serra, Phys. Rev. B **98**, 121407 (2018)
66. Y.-T. Zhang, Z. Hou, X. C. Xie, et al., Phys. Rev. B **95**, 245433 (2017)
67. Y.-F. Zhou, Z. Hou, Y.-T. Zhang, et al., Phys. Rev. B **97**, 115452 (2018)
68. T. O. Rosdahl, A. Vuik, M. Kjaergaard, et al., Phys. Rev. B **97**, 045421 (2018)
69. R. W. Reinthaler, P. Recher, E. M. Hankiewicz, Phys. Rev. Lett. **110**, 226802 (2013)
70. A. R. Akhmerov, J. Nilsson, C. W. J. Beenakker, Phys. Rev. Lett. **102**, 216404 (2009)
71. L. Fu, C. L. Kane, Phys. Rev. Lett. **102**, 216403 (2009)
72. H. S. Røising, S. H. Simon, Phys. Rev. B **97**, 115424 (2018)
73. J. Osca, L. Serra, Physica Status Solidi C **12(12)**, 1409 (2015)
74. D. Ruiz, J. Osca, L. Serra, Journal of Physics: Condensed Matter **27**, 12, 125302 (2015)
75. J. Osca, L. Serra, Beilstein J. Nanotechnol. **9**, 1194 (2018)